

# Near-Field Wideband Beamforming for Extremely Large Antenna Arrays

Mingyao Cui, *Graduate Student Member, IEEE*, Linglong Dai, *Fellow, IEEE*

**Abstract**—The natural integration of extremely large antenna arrays (ELAAs) and terahertz (THz) communications can potentially establish Tbps data links for 6G networks. However, due to the extremely large array aperture and wide bandwidth, a new phenomenon termed as “near-field beam split” emerges. This phenomenon causes beams at different frequencies to focus on distinct physical locations, leading to a significant loss of the beamforming gain. To address this challenging problem, we first harness a piecewise-far-field channel model to approximate the complicated near-field wideband channel. In this model, the entire large array is partitioned into several small sub-arrays. While the wireless channel’s phase discrepancy across the entire array is modeled as near-field spherical, the phase discrepancy within each sub-array is approximated as far-field planar. Built on this approximation, a phase-delay focusing (PDF) method employing delay phase precoding (DPP) architecture is proposed. Our PDF method could compensate for the intra-array far-field phase discrepancy and the inter-array near-field phase discrepancy via the joint control of phase shifters and time delayers, respectively. Theoretical and numerical results are provided to demonstrate the efficiency of the proposed PDF method in mitigating the near-field beam split effect. Finally, we define and derive a novel metric termed as the “effective Rayleigh distance” by the evaluation of beamforming gain loss. Compared to classical Rayleigh distance, the effective Rayleigh distance is more accurate in determining the near-field range for practical communications.

**Index Terms**—Extremely large antenna array, wideband, near-field beam split, beamforming, Rayleigh distance.

## I. INTRODUCTION

As a key technology for 5G communication systems, large antenna arrays (LAAs) could improve the transmission rate by orders of magnitude via efficient beamforming/precoding [1]. To further reap the benefits of massive antennas, LAAs are evolving to extremely large antenna arrays (ELAAs) for 6G communications [2], where the array aperture is dramatically increased to support ultra-high-speed communications. There are abundant possible implementations of ELAA. For instance, ELAA could be employed in distributed multiple-input-multiple-output (MIMO) systems relying on radio stripes [3] or in reconfigurable intelligent surface (RIS) systems [4] to improve the network capacity. It is also envisioned to coat ELAAs on entire walls to enhance the coverage of wireless signals [5].

All authors are with the Department of Electronic Engineering, Tsinghua University, Beijing 100084, China (e-mails: cui-my16@tsinghua.org.cn, daill@tsinghua.edu.cn).

This work was funded in part by the National Science Fund for Distinguished Young Scholars (Grant No. 62325106), and in part by the National Key R&D Program of China (No. 2023YFB3811503). (*Corresponding author: Linglong Dai.*)

In addition, ELAAs are usually combined with high-frequency communications. Benefiting from the abundant spectrum resources, terahertz (THz) communications can provide a very large bandwidth of several GHz, allowing for Tbps data rates for 6G networks [6]. Besides, the extremely small size of THz antennas also favorably facilitates the deployment of ELAAs [7]. As a consequence, the natural integration of THz wideband communications and ELAAs has been regarded as a pivotal candidate for next-generation wireless networks [7].

### A. Prior Works

The evolution from LAA to ELAA not only implies a sharp increment in array aperture, but also leads to a fundamental change in the characteristics of the electromagnetic (EM) field [8]. The electromagnetic radiation field can generally be divided into the far-field and radiation near-field regions [9], [10]. In the far-field region, the wireless channel could be modeled under the **planar** wave assumption, where the phase of the array response vector is a *linear* function of the antenna index [11], [12]. In contrast, the wavefront of near-field channel has to be modeled accurately as **spherical**, where the phase of near-field array response vector is a *non-linear* function of the antenna index [9]. The boundary between near-field and far-field is typically quantified by the Rayleigh distance [9], also known as the Fraunhofer distance [13], which is proportional to the square of array aperture normalized by wavelength. Since the array aperture is typically not very large in the current 5G systems, the near-field range of 5G LAA is negligible. That is why classical beamforming techniques usually direct a beam with planar wavefront in a specific direction [1]. In contrast, as the number of ELAA’s antennas increases dramatically, the Rayleigh distance will be expanded by orders of magnitude. The near-field range of an ELAA could be up to several hundreds of meters [8], covering a large part of typical cells. In this scenario, it is necessary to perform near-field beamforming to focus the energy of a beam on a desired user location [14] by exploiting the spherical wavefront property. Given this non-negligible near-field range, near-field communications will be of pivotal significance in next-generation communications.

Moreover, when it comes to wideband systems, another critical change in EM waves known as beam split is induced, which also has the terminology “beam squint” [15], [16]. Classically, LAA relies on phased shifter (PS) based analog beamforming architecture, allowing only *frequency-independent* phase shifting for narrowband beamforming [17].

However, the array response vectors of wireless channels are *frequency-dependent*, especially for THz wideband networks, causing the wavefront of a beam at different frequencies to deviate from that at the center frequency. To elaborate, in far-field scenarios, the beam split effect makes beams of different frequency components propagate in distinct directions [15]. On the other hand, in near-field scenarios, the beam split effect results in a new phenomenon where beams at different frequencies are focused at varying directions and distances. Consequently, the signal energy fails to converge on the desired receiver's location. Only signals around the center frequency can be captured by the receiver, while most beams with frequencies far away from the center frequency suffer from an unacceptable beamforming gain loss.

Over the past few years, intensive research has been devoted to studying advanced beamforming technologies to address the far-field beam split effect [16], [18]–[22]. Relevant methods fall into two primary categories, i.e., algorithmic methods and hardware-based mitigation methods. In the first category, researchers have endeavored to generate wide beams by carefully optimizing the PSs to achieve flattened beamforming gain across the entire bandwidth [16], [18], [19]. While these algorithms are relatively straightforward to implement in practice, their beamforming performance is severely hindered by the presence of beam split as well. This limitation arises because they still rely on PS-based analog beamforming. The second category of solutions employs true-time-delay (TTD) circuits instead of PSs to generate *frequency-dependent* beams, which offers the potential to eliminate far-field beam split [20]–[22]. Inspired by this idea, several array structures, such as true-time-delay (TTD) arrays [20] and delay-phase precoding (DPP) arrays [21], [22], have been envisioned and developed to counteract the far-field beam split effect. Despite the rapid development of solutions to far-field beam split, it is essential to note that the aforementioned methods are all customized for far-field communications. They are not applicable to tackle the challenges posed by near-field beam split, because the models of far-field channels and near-field channels differ remarkably. To the best of our knowledge, the near-field beam split effect has not been studied in the literature.

## B. Our Contributions

To fill in this gap, a phase-delay focusing (PDF) method is proposed to tackle the near-field beam split problem<sup>1</sup>. Our key contributions are summarized as follows.

- First, we introduce the near-field beam split effect of ELAA by comparing the loss of beamforming gain resulting from both far-field and near-field beam split effects. We formulate the model of near-field beam split effect and reveal that this effect causes beams at different frequencies to focus on distinct locations.
- Second, a piecewise-far-field wideband channel model is proposed to approximate the near-field wideband channel model with high accuracy. In this model, the entire ELAA is partitioned into multiple small sub-arrays. In

this way, we could reasonably assume that the receiver is located in the far-field region of each small sub-array while being in the near-field region of the entire ELAA. This partition allows us to decompose the complicated phase discrepancy of a near-field channel into two distinct components: the inter-array near-field phase discrepancy and the intra-array far-field phase discrepancy. Leveraging this decomposition, a phase-delay focusing (PDF) method is proposed based on the DPP array architecture, where the inter-array phase and the intra-array phase are compensated by the PSs and TTDs of DPP, respectively. Simulation results validate the efficacy of the proposed PDF method in mitigating the near-field beam split effect.

- Finally, by evaluating the gain loss of far-field beamforming in the near-field region, a new metric called effective Rayleigh distance is defined to distinguish the far-field and near-field regions. Classical Rayleigh distance, which is defined by evaluating the phase error between planar wave and spherical wave, is not precise enough to capture the near-field region where far-field beamforming methods are not applicable. To tackle this problem, we conduct a theoretical evaluation on the gain loss of far-field beamforming in the physical space. Subsequently, the close-form expression of effective Rayleigh distance is derived, which defines the region where the gain loss of far-field beamforming exceeds a threshold. Since beamforming gain directly affects the received signal power, our proposed effective Rayleigh distance is a more accurate metric for measuring the near-field range for practical communications.

## C. Organization and notation

The rest of the paper is organized as follows. In section II, the wideband ELAA channel model is introduced and the near-field beam split effect is discussed. In section III, the proposed piecewise-far-field channel model and the proposed PDF method are explained in detail. Theoretical analysis on the beamforming gain of the PDF method is also offered. Section IV elaborates on the effective Rayleigh distance. Numerical results are provided in section V. Finally, conclusions are drawn in section VI.

*Notation:* Lower-case boldface letters  $\mathbf{x}$  denote vectors;  $(\cdot)^T$ ,  $(\cdot)^H$ ,  $(\cdot)^*$  and  $\|\cdot\|_k$  denote the transpose, conjugate transpose, conjugate, and  $k$ -norm of a vector or matrix respectively;  $|x|$  denotes the amplitude of scalar  $x$ ;  $\arg(x)$  denotes the phase of  $x$ ;  $[\mathbf{x}]_n$  represents the  $n^{\text{th}}$  element of vector  $\mathbf{x}$ ;  $[\mathbf{X}]_{ij}$  represents the  $(i, j)^{\text{th}}$  entry of matrix  $\mathbf{X}$ ;  $\mathcal{CN}(\mu; \Sigma)$  and  $\mathcal{U}(a; b)$  denote the Gaussian distribution with mean  $\mu$  and covariance  $\Sigma$ , and the uniform distribution between  $a$  and  $b$ , respectively;  $\Xi_N(x)$  denotes the Dirichlet sinc function  $\Xi_N(x) = \frac{\sin(\frac{N}{2}\pi x)}{N \sin(\frac{1}{2}\pi x)}$ .

## II. NEAR-FIELD BEAM SPLIT

In this section, we elaborate on the near-field beam-split effect in wideband ELAA systems. We will first introduce the system model based on the conventional hybrid beamforming architecture, and then the near-field beam split effect is discussed from this model.

<sup>1</sup>Simulation codes are provided to reproduce the results presented in this article: <http://oa.ee.tsinghua.edu.cn/dailong/publications/publications.html>.

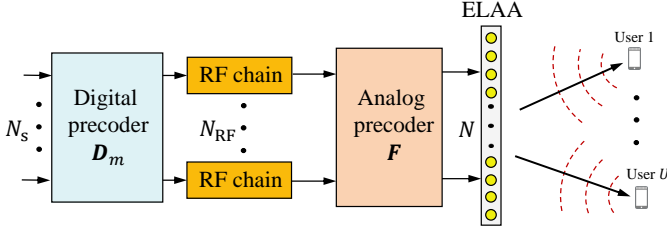


Fig. 1. The system layout of ELAA.

### A. System Model

In our system, a base station (BS) equipped with an  $N$ -element uniform linear array (ULA) serves  $U$  single-antenna users. The BS employs the fully connected hybrid beamforming architecture with  $N_{\text{RF}}$  radio frequency (RF) chains, each connected to all antennas via analog phase shifters. To reap the multiplexing gain,  $U$  data streams are simultaneously transmitted, where  $U \leq N_{\text{RF}} \ll N$ . In this article, we assume  $U = N_{\text{RF}}$  for illustration simplicity. The orthogonal frequency division multiplexing (OFDM) with  $M$  sub-carriers is adopted. Variables  $d = \frac{\lambda_c}{2}$ ,  $\lambda_c$ ,  $c$ ,  $f_c = \frac{c}{\lambda_c}$ , and  $B$  denote the antenna spacing, carrier wavelength, speed of light, center carrier, bandwidth, respectively. Besides, let  $f_m = f_c + \frac{B}{2}(\frac{2}{M-1}m-1)$  for  $m \in \{0, 1, \dots, M-1\}$  be the  $m^{\text{th}}$  subcarrier frequency. Accordingly, the user-side received signal  $\mathbf{y}_m \in \mathbb{C}^{U \times 1}$  on the  $m^{\text{th}}$  subcarrier is expressed as

$$\mathbf{y}_m = \sqrt{\rho} \mathbf{H}_m^T \mathbf{F} \mathbf{D}_m + \mathbf{n}_m, \quad (1)$$

where  $\mathbf{H} \in \mathbb{C}^{N \times U}$ ,  $\mathbf{F} \in \mathbb{C}^{N \times N_{\text{RF}}}$ , and  $\mathbf{D}_m \in \mathbb{C}^{N_{\text{RF}} \times U}$  represent the channel matrix, the analog beamformer, and the digital precoder respectively. It is noticeable that since the digital precoding is carried out subcarrier-by-subcarrier on the digital baseband, the digital precoder  $\mathbf{D}_m$  is frequency-dependent. However, the analog precoder realized by PSs can only tune a uniform phase for all subcarriers, making  $\mathbf{F}$  frequency-independent. Taking into account the circuit restriction, each entry of  $\mathbf{F}$  satisfies the constant modulus constraint, i.e.,  $|\mathbf{F}_{i,j}| = \frac{1}{\sqrt{N}}$ . The noise  $\mathbf{n}_m$  follows the complex Gaussian distribution  $\mathcal{CN}(0, \sigma^2 \mathbf{I})$ .

We denote the channel matrix as  $\mathbf{H}_m = [\mathbf{h}_{0,m}, \mathbf{h}_{1,m}, \dots, \mathbf{h}_{U-1,m}]$ , where vector  $\mathbf{h}_{u,m}$  stands for the wireless channel from the BS to the  $u^{\text{th}}$  user. As shown in Fig. 1, the center of the BS array is located at  $(0,0)$  in the Cartesian coordinates, and then the coordinate of the  $n^{\text{th}}$  BS antenna is  $(0, \delta_N^{(n)} d)$ , where  $\delta_N^{(n)} = n - \frac{N-1}{2}$  with  $n \in \{0, 1, \dots, N-1\}$ . Therefore, the array aperture is given as  $D = (N-1)d \approx Nd$ . The  $u^{\text{th}}$  user is located at  $(x_u, y_u)$ , where its polar coordinate is  $(r_u, \theta_u) = (\sqrt{x_u^2 + y_u^2}, \arctan \frac{y_u}{x_u})$ . Then, adopting the free space Maxwell equation, the line-of-sight near-field channel  $\mathbf{h}_{u,m}$  can be modeled [9] as

$$\begin{aligned} \mathbf{h}_{u,m} &= g_{u,m} \left[ e^{-jk_m r_u^{(0)}}, e^{-jk_m r_u^{(1)}}, \dots, e^{-jk_m r_u^{(N-1)}} \right]^T \\ &= g_{u,m} \sqrt{N} \mathbf{a}_m(r_u, \theta_u), \end{aligned} \quad (2)$$

where  $\mathbf{a}_m(r_u, \theta_u)$  represents the near-field array response vector,  $k_m = \frac{2\pi f_m}{c}$  denotes the wavenumber at frequency  $f_m$ ,

and  $g_m$  denotes the complex path loss. Let  $r_u^{(n)}$  be the distance from the  $n^{\text{th}}$  BS antenna to the  $u^{\text{th}}$  user expressed as

$$\begin{aligned} r_u^{(n)} &= (x_u^2 + (y_u - \delta_N^{(n)} d)^2)^{\frac{1}{2}} \\ &= (r_u^2 + (\delta_N^{(n)} d)^2 - 2\delta_N^{(n)} d r_u \sin \theta_u)^{\frac{1}{2}}. \end{aligned} \quad (3)$$

Since the PS-based analog beamformer  $\mathbf{F}$  is frequency-independent, each column of  $\mathbf{F}$  is generally set to align with the array response vector of the wireless channel at the center frequency  $f_c$  [1], [23]. Thereafter, let  $\mathbf{F} = [\mathbf{f}_0, \mathbf{f}_1, \dots, \mathbf{f}_{U-1}]$ , then  $\mathbf{f}_u$  can be obtained by

$$\mathbf{f}_u = \mathbf{a}_c^*(r_u, \theta_u) = \frac{1}{\sqrt{N}} [e^{jk_c r_u^{(0)}}, \dots, e^{jk_c r_u^{(N-1)}}]^T, \quad (4)$$

where  $k_c = \frac{2\pi f_c}{c}$  and  $\mathbf{a}_c^*(r_u, \theta_u)$  represent the wavenumber and array response vector on the center frequency  $f_c$ . The fundamental model difference from the near-field array response vector  $\mathbf{a}_m(r_u, \theta_u)$  to the analog beamformer  $\mathbf{f}_u = \mathbf{a}_c^*(r_u, \theta_u)$  causes the near-field beam split effect.

### B. Discussion on Near-Field Beam Split

To delve into the near-field beam split effect, we would like to compare the beamforming properties under far-field/near-field and narrowband/widband conditions. In the upcoming discussions, we will omit the subscript  $u$  for ease of expression. Notice that the phase  $k_m r^{(n)}$  in (2) and  $k_c r^{(n)}$  in (4) are non-linear functions with respect to (w.r.t) the antenna index  $n$ . Traditionally, since the array aperture is not very large, the far-field model under the planar wave assumption [11] is widely adopted to simplify this non-linear distance as

$$\begin{aligned} r^{(n)} &= r \left( 1 + \frac{(\delta_N^{(n)} d)^2}{r^2} - \frac{2\delta_N^{(n)} d \sin \theta}{r} \right)^{\frac{1}{2}} \\ &\stackrel{(a)}{\approx} r \left( 1 - \frac{\delta_N^{(n)} d \sin \theta}{r} \right) = r - \delta_N^{(n)} d \sin \theta, \end{aligned} \quad (5)$$

where (a) arises because of the first-order Taylor expansion  $(1+x)^{\frac{1}{2}} \approx 1 + \frac{1}{2}x$  and the ignorance of the second-order term  $\frac{(\delta_N^{(n)} d)^2}{r^2}$ . It is clear from (5) that in the far-field region, the phase becomes  $k_m r^{(n)} \approx k_m r - k_m \delta_N^{(n)} d \sin \theta$ , which is a linear function of the antenna index  $n$ . Then the far-field beamforming vector becomes  $[\mathbf{f}]_n = \frac{1}{\sqrt{N}} e^{jk_c r} e^{-jk_c \delta_N^{(n)} d \sin \theta}$ . Because the term  $e^{jk_c r}$  is independent of the antenna index  $n$ ,  $[\mathbf{f}]_n$  can be rewritten as  $[\mathbf{f}]_n = \frac{1}{\sqrt{N}} e^{-jk_c \delta_N^{(n)} d \sin \theta} = [\mathbf{f}^{\text{far}}(\theta)]_n$ , depending only on direction  $\theta$ . As shown in Fig. 2 (a), the beam at the center frequency generated by  $[\mathbf{f}^{\text{far}}(\theta)]_n$  is transmitting towards a specific direction  $\theta$ .

However, since the linear approximation in (5) is not accurate when  $n$  is very large, the above far-field assumption does not hold anymore for ELAAs. The typical near-field range is determined by the Rayleigh distance [24]  $R = \frac{2D^2}{\lambda_c} = \frac{1}{2} N^2 \lambda_c$ . If the number of antennas  $N$  increases dramatically, the near-field region will expand by orders of magnitude. For instance, for a 512-antenna ULA operating at 100 GHz frequency, the Rayleigh distance is about 400 meters. In this case, the accurate spherical wave model has to be adopted for the channel  $\mathbf{h}_m$  in (2) and the beamforming vector  $\mathbf{f}$  in (4).

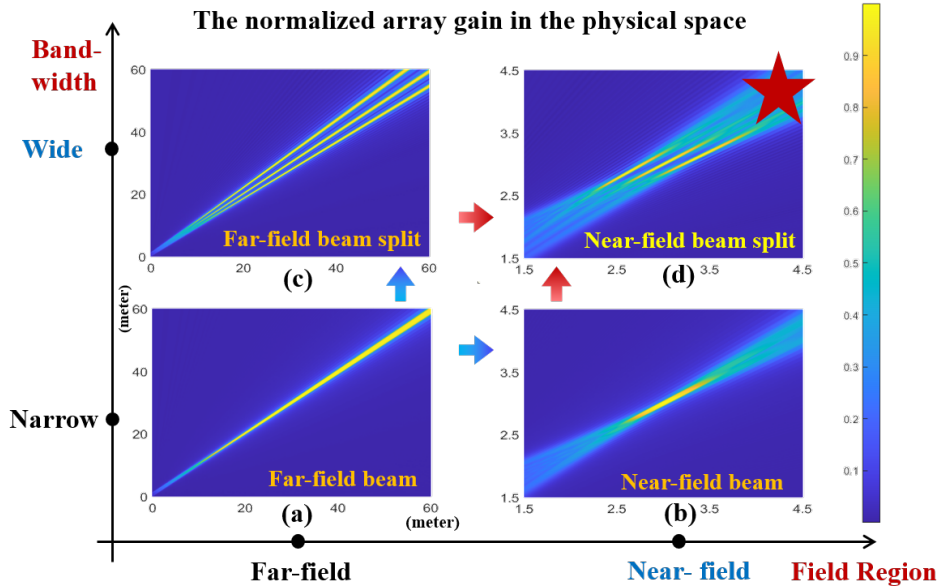


Fig. 2. This figure illustrates the normalized beamforming gain in the physical space. We consider four scenarios: (a) the far-field narrowband scenario, (b) the near-field narrowband scenario, (c) the far-field wideband scenario, and (d) the near-field wideband scenario. In each sub-figure, the beam energy of the lowest, the center, and the highest frequencies are plotted (e.g., the three lines in the sub-figures (c) and (d)).

Accordingly, as shown in Fig. 2 (b), the energy of near-field beam at the center frequency is focused on the location  $(r, \theta)$  [23], which depends on both the distance  $r$  and direction  $\theta$  of the receiver. Therefore, near-field beamforming also has the terminology “beamfocusing” in the literature [14], [25].

The discussion above assumes that the bandwidth is not very large. As for wideband systems, a severe beam split effect is induced. Specifically, employing the beamforming vector  $\mathbf{f} = \mathbf{a}_c^*(r, \theta)$ , we define  $G(\hat{r}, \hat{\theta}, r, \theta, f_m) = |\mathbf{a}_m^T(\hat{r}, \hat{\theta})\mathbf{f}|$  as the normalized beamforming gain at frequency  $f_m$  on the location  $(\hat{r}, \hat{\theta})$  with  $\hat{r}^{(n)} = \sqrt{\hat{r}^2 + (\delta_N^{(n)} d)^2} - 2\delta_N^{(n)} d \hat{r} \hat{\theta}$ . According to (2), we have

$$G(\hat{r}, \hat{\theta}, r, \theta, f_m) = \frac{1}{N} \left| \sum_{n=0}^{N-1} e^{-j(k_m \hat{r}^{(n)} - k_c r^{(n)})} \right|. \quad (6)$$

Clearly, the maximum value of  $G(\hat{r}, \hat{\theta}, r, \theta, f_m)$  is 1. In narrowband systems where  $f_m \approx f_c$ , the beamforming gain  $G(\hat{r}, \hat{\theta}, r, \theta, f_m)$  reaches its zenith when  $(\hat{r}, \hat{\theta}) = (r, \theta)$ , signifying that the beam energy is precisely focused at location  $(r, \theta)$ . However, in wideband systems, when  $f_m \neq f_c$  and  $(\hat{r}, \hat{\theta}) = (r, \theta)$ , the elements  $e^{-j(k_c - k_m)r^{(n)}}$  exhibit diverse phases, preventing them from being constructively added up on the user location. This phenomenon substantially reduces the beamforming gain  $G(\hat{r}, \hat{\theta}, r, \theta, f_m)|_{(\hat{r}, \hat{\theta})=(r, \theta)}$ , rendering it much lower than 1. Consequently, the beam energy at  $f_m$  is split from the desired location  $(r, \theta)$  [26]. In the far-field scenario where the distance is considerable, as shown in Fig. 2 (c), this beam split effect causes beams at different frequencies to transmit towards *different directions*. However, in the near-field setting, as shown in Fig. 2 (d), the near-field beam split effect causes beams at different frequencies to focus on *different locations*. These distinct beamforming properties

distinguish the far-field and near-field beam split effects<sup>2</sup>.

Furthermore, since beams over large bandwidth are split to different locations/directions, the user can only access to signals close to the center frequency. For example, considering  $f_c = 100$  GHz,  $B = 5$  GHz, and  $N = 512$ , the near-field beam-split effect results in over 50% of the sub-carriers experiencing a beamforming gain loss of at least 60%. Recent works mainly concentrate on mitigating the far-field beam-split effect. This is accomplished by either deploying a large number of high power consumption time-delay elements [27], [20] or heavily relying on the linear phase property of the far-field channel [16], [18], [19], [21], which is not applicable in the near field. To the best of our knowledge, the near-field beam-split effect has not been studied in the literature.

### III. PROPOSED METHODS

In this section, we commence by introducing a piecewise-far-field channel characterized by piecewise-linear phase properties to approximate the intricate near-field channel. Subsequently, a PDF method is built on this approximation to mitigate the near-field beam split effect.

#### A. Piecewise-Far-Field Channel Model

The non-linear phase  $-k_m r_u^{(n)}$  w.r.t the antenna index  $n$  makes it intractable to directly devise near-field wideband beamforming techniques. In order to get a manageable simplification of this non-linear phase while maintaining acceptable accuracy, we observe that the Rayleigh distance  $\frac{1}{2}N^2\lambda_c$  scales proportionally with the square of the number of antennas, signifying that fewer antennas corresponds to a better accuracy of the far-field assumption in (5).

<sup>2</sup>Notice that the sub-figures (c) and (d) of Fig. 2 also appear in our earlier work [26], where [26] employs near-field beam split to perform fast beam training, while the objective of this work is to mitigate this phenomenon via energy-efficient beamforming.

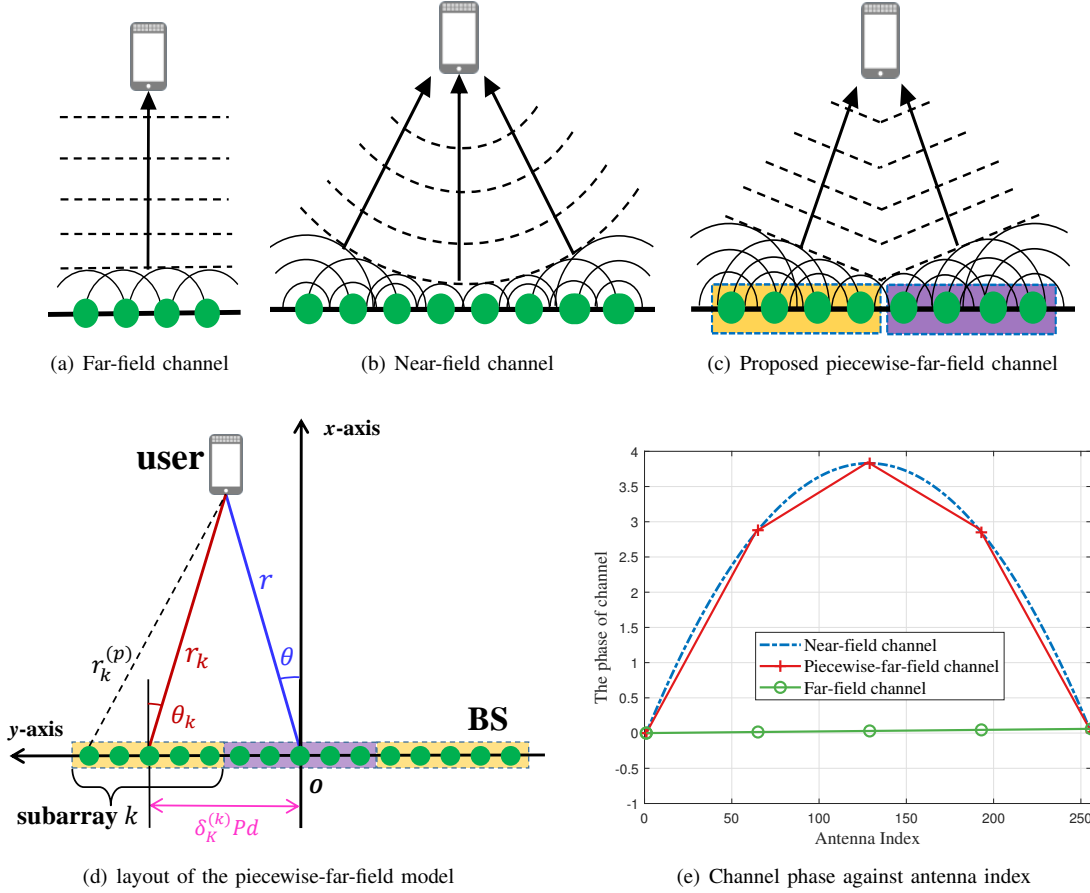


Fig. 3. Schematic diagrams of (a) far-field channel model, (b) near-field channel model, (c) piecewise-far-field channel model, (d) layout of the piecewise-far-field model, and (e) channel phase against the antenna index. The number of antennas is 256, the carrier frequency is 100 GHz. The user is located at  $(x, y) = (10 \text{ m}, 0 \text{ m})$ . With  $K = 4$  sub-arrays, the piecewise-far-field channel can well approximate the near-field channel model.

Inspired by this observation, as depicted in Fig. 3 (a)-(c), a piecewise-far-field channel model is harnessed to approximate the intricate near-field channel. In this model, the entire large array is partitioned into multiple sub-arrays, each equipped with much fewer antennas compared to the entire array. This partition leads to a notable reduction of the near-field range for each sub-array. Consequently, even if the receiver is inside the near-field region of the entire array, we can reasonably assume that the receiver is situated in the far-field region of each sub-array.

To elaborate, as shown in Fig. 3 (d), we divide the entire large array into  $K$  sub-arrays. For each sub-array, there are  $P$  adjacent antennas, satisfying  $N = KP$ . Then, the near-field channel from the BS to the  $u^{\text{th}}$  user is rearranged as follows

$$\mathbf{h}_{u,m} = \left[ \mathbf{h}_{u,m}^{(0)T}, \mathbf{h}_{u,m}^{(1)T}, \dots, \mathbf{h}_{u,m}^{(K-1)T} \right]^T, \quad (7)$$

where  $\mathbf{h}_{u,m}^{(k)} \in \mathbb{C}^{P \times 1}$  represents the sub-channel between the  $k^{\text{th}}$  sub-array and the  $u^{\text{th}}$  user. We define  $\delta_K^{(k)} = k - \frac{K-1}{2}$  for  $k \in \{0, 1, \dots, K-1\}$ . Then, the distance and direction from the center of the  $k^{\text{th}}$  sub-array to the  $u^{\text{th}}$  user are expressed as  $r_{u,k} = \sqrt{x_u^2 + (y_u - \delta_K^{(k)} P d)^2} = \sqrt{r_u^2 + (\delta_K^{(k)} P d)^2 - 2\delta_K^{(k)} P d r_u \sin \theta_u}$  and  $\sin \theta_{u,k} = \frac{y_u - \delta_K^{(k)} P d}{r_{u,k}}$ , respectively. We further define  $\delta_P^{(p)} = p - \frac{P-1}{2}$

for  $p \in \{0, 1, \dots, P-1\}$ . Subsequently, according to (5), the distance  $r_{u,k}^{(p)}$  from the  $p^{\text{th}}$  antenna in the  $k^{\text{th}}$  sub-array to the  $u^{\text{th}}$  user is expressed as

$$\begin{aligned} r_{u,k}^{(p)} &= \sqrt{r_{u,k}^2 + (\delta_P^{(p)} d)^2 - 2\delta_P^{(p)} d r_{u,k} \sin \theta_{u,k}} \\ &\approx r_{u,k} - \delta_P^{(p)} d \sin \theta_{u,k}. \end{aligned} \quad (8)$$

There, the approximation (a) holds because each sub-array is small enough. Accordingly, the near-field channel  $\mathbf{h}_{u,m}^{(k)}$  of the  $k^{\text{th}}$  sub-array is approximated by a far-field channel  $\tilde{\mathbf{h}}_{u,m}^{(k)}$ :

$$[\mathbf{h}_{u,m}^{(k)}]_p \approx g_{u,m} e^{-jk_m r_{u,k}} e^{jk_m \delta_P^{(p)} d \sin \theta_{u,k}} = [\tilde{\mathbf{h}}_{u,m}^{(k)}]_p. \quad (9)$$

By introducing the parameter  $\eta_m = \frac{f_m}{f_c}$  and plugging  $d = \frac{\lambda_c}{2} = \frac{c}{2f_c}$  and  $k_m = \frac{2\pi f_m}{c}$  into (9), we arrive at  $[\tilde{\mathbf{h}}_{u,m}^{(k)}]_p = e^{-jk_m r_{u,k}} e^{j\pi \eta_m \delta_P^{(p)} \sin \theta_{u,k}}$ . Consequently, the intricate near-field channel is approximated by a piecewise-far-field channel:

$$\mathbf{h}_{u,m} \approx \tilde{\mathbf{h}}_{u,m} = \left[ \tilde{\mathbf{h}}_{u,m}^{(0)}, \tilde{\mathbf{h}}_{u,m}^{(1)}, \dots, \tilde{\mathbf{h}}_{u,m}^{(K-1)} \right]. \quad (10)$$

It is notable from (9) that the phase of  $[\tilde{\mathbf{h}}_{u,m}^{(k)}]_p$  is a linear function of  $p$ , the antenna index of the  $k^{\text{th}}$  sub-array. This linear phase property suggests that  $[\tilde{\mathbf{h}}_{u,m}^{(k)}]_p$  can be regarded as a far-field channel. Furthermore, considering the different  $r_k$  and  $\theta_k$  in each sub-array, the planar waves impinging

on different sub-arrays come from different directions. This is why we call the entire array's channel the piecewise-far-field channel. To illustrate the fidelity of the proposed model, Fig. 3 (e) depicts the channel phase as a function of the antenna index for the near-field, far-field, and piecewise-far-field channel models. The phase profile of the piecewise-far-field channel model closely approaches that of the true near-field channel. In essence, our proposed channel model can be recognized as a piecewise-linearization of the intricate near-field channel model, wherein the phase exhibits local linear behavior within each sub-array. Harnessing this piecewise-linear phase characteristics, we proceed to devise a near-field wideband beamforming method referred to as phase-delay focusing to alleviate the near-field beam-split effect in the subsequent subsection.

### B. Proposed Phase-Delay Focusing Method

We first elaborate on overcoming the near-field beam-split for an arbitrary user by analog beamforming, while the extension to multi-user hybrid beamforming is studied in Section III-D. For ease of expression, the subscript  $u$  is omitted in Section III-B to III-C. Accordingly, the variables  $\mathbf{h}_{u,m}$ ,  $\tilde{\mathbf{h}}_{u,m}$ ,  $\mathbf{f}_u$ ,  $r_u$ ,  $\theta_u$ ,  $r_{u,k}$ , and  $\theta_{u,k}$  become  $\mathbf{h}_m$ ,  $\tilde{\mathbf{h}}_m$ ,  $\mathbf{f}$ ,  $r$ ,  $\theta$ ,  $r_k$ , and  $\theta_k$ .

Specifically, the introduced piecewise-far-field channel model makes it straightforward to decouple the phase in (9) into two components: the inter-array phase discrepancy  $-k_m r_k$  across different sub-arrays, and the intra-array phase discrepancy  $\pi \eta_m \delta_P^{(p)} \sin \theta_k$  within each sub-array. It is notable that  $-k_m r_k$  is a non-linear function of  $k$ , giving rise to a near-field channel phase property, whereas  $\pi \eta_m \delta_P^{(p)} \sin \theta_k$  follows a linear function in relation to  $p$ , as the same to a far-field model. Both of these two phase components contribute to the near-field beam split effect. The following fact inspires us to neglect the influence of intra-array phase  $\pi \eta_m \delta_P^{(p)} \sin \theta_k$  on near-field beam split. As suggested in [21], [28], the degree of beam-split effect is proportional to the physical antenna aperture. A larger antenna aperture results in a severer beam-split effect. Although this conclusion is derived in the far-field region, it is valid to near-field as well, because the physical propagation delay always increases with the antenna aperture, no matter far-field or near-field. Following this intuition, we can find that the intra-array phase discrepancy  $k_m \delta_P^{(p)} d \sin \theta_k$  corresponds to a sub-array's aperture  $Pd$ , while the inter-array phase discrepancy  $k_m r_k$  is related to the entire array's aperture  $Nd$ . Since  $P \ll N$ , it is reasonable to deduce the near-field beam split is dominated by the inter-array phase discrepancy. Consequently, our target is converted to compensating for the inter-array phase  $-k_m r_k$ .

Note that the channel phase  $-k_m r_k = -\frac{2\pi f_m r_k}{c}$  is equivalent to the frequency response of a time delay of  $\frac{r_k}{c}$ . Therefore, the delay-phase precoding architecture [21] employing TTD circuits can be used to compensate for the inter-array phase  $-k_m r_k$ . As illustrated in Fig. 4, compared to conventional hybrid precoding architecture, one additional TTD circuit is inserted in each sub-array to connect the RF chain and the PS-based sub-array. The frequency response of a TTD at  $f_m$  is  $e^{-j2\pi f_m \tau'}$ , where  $\tau'$  represents the adjustable time

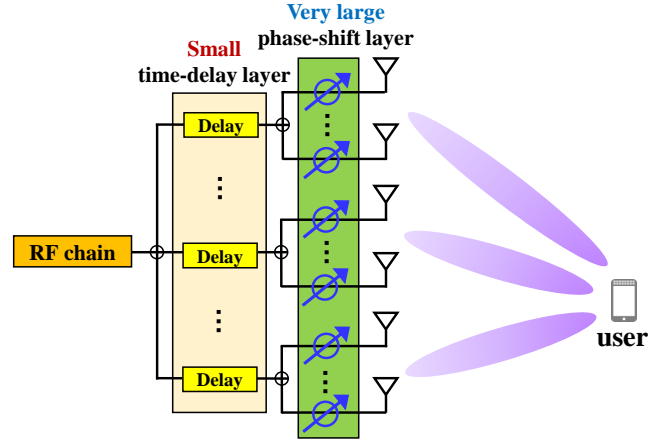


Fig. 4. A single-user example of the delay-phase precoding architecture [21] for performing the PDF method.

delay parameter. For brevity, let  $r' = c\tau'$  be the adjustable distance parameter. Then, the corresponding frequency response is transformed into  $e^{-jk_m r'}$ . Thereby, a TTD is able to compensate for the frequency-dependent phase  $-k_m r_k$  if  $r' = -r_k$ . Moreover, as shown in Fig. 4, the main function of the PS-based sub-array is to generate far-field planar waves to match the intra-array far-field phase  $\pi \eta_m \delta_P^{(p)} \sin \theta_k$ . Through the joint manipulation of PSs and TTDs, the beam energy across the entire bandwidth can be focused on the receiver location  $(r, \theta)$ . We henceforth refer to this method as phase-delay focusing.

Recall that the analog beamformer  $\mathbf{f}$  realized by PS is frequency-independent. In contrast, the introduction of TTD makes the corresponding analog beamformer  $\mathbf{f}_m$  frequency-dependent. To be specific, similar to the decomposition of wireless channel presented in (7), the beamforming vector  $\mathbf{f}_m$  realized by the PDF method at  $f_m$  is composed of  $K$  sub-vectors, i.e.,

$$\mathbf{f}_m = \left[ \mathbf{f}_m^{(0)T}, \mathbf{f}_m^{(1)T}, \dots, \mathbf{f}_m^{(K-1)T} \right]^T, \quad (11)$$

where  $\mathbf{f}_m^{(k)} \in \mathbb{C}^{P \times 1}$  represents the beamforming vector of the  $k^{\text{th}}$  sub-array. As illustrated in Fig. 4,  $\mathbf{f}_m^{(k)}$  is generated by one TTD element and  $P$  PSs, which can be expressed as follows:

$$\mathbf{f}_m^{(k)} = \frac{1}{\sqrt{N}} e^{-jk_m r'_k} \left[ e^{j\pi \delta_P^{(0)} \beta'_k}, \dots, e^{j\pi \delta_P^{(P-1)} \beta'_k} \right]^T. \quad (12)$$

Here,  $r'_k$  denotes the adjustable distance parameter of the  $k^{\text{th}}$  TTD element and  $\beta'_k$  denotes the adjustable phase parameter associated with the  $k^{\text{th}}$  PS-based sub-array. It is evident from (12) that  $\mathbf{f}_m^{(k)}$  includes two distinct components. The first one is the frequency-independent phase  $\pi \delta_P^{(p)} \beta'_k$  generated by the  $P$  PSs within the  $k^{\text{th}}$  sub-array. The second one involves the frequency-dependent phase  $-k_m r'_k$  realized by the  $k^{\text{th}}$  TTD element. As discussed earlier, the purpose of  $\pi \delta_P^{(p)} \beta'_k$  is to produce planar waves that align with the far-field phase discrepancy  $\pi \eta_m \delta_P^{(p)} \sin \theta_k$ , while the introduction of  $t'_k = \frac{r'_k}{c}$  serves to compensate for the near-field phase discrepancy  $-k_m r_k$ .

To elaborate, the normalized beamforming gain achieved by the proposed PDF method on the user location is expressed as

$$\begin{aligned} G_m &= \frac{1}{\sqrt{|g_m|N}} \left| \tilde{\mathbf{h}}_m^T \mathbf{f}_m \right| = \frac{1}{\sqrt{|g_m|N}} \left| \sum_{k=0}^{K-1} \tilde{\mathbf{h}}_m^{(k)T} \mathbf{f}_m^{(k)} \right| \\ &= \frac{1}{N} \left| \sum_{k=0}^{K-1} e^{-jk_m(r'_k+r_k)} \sum_{p=0}^{P-1} e^{j\delta_P^{(p)} \pi(\beta'_k + \eta_m \sin \theta_k)} \right| \\ &= \frac{1}{K} \left| \sum_{k=0}^{K-1} e^{-jk_m(r'_k+r_k)} \Xi_P(\beta'_k + \eta_m \sin \theta_k) \right|, \quad (13) \end{aligned}$$

where  $\Xi_P(x) = \frac{\sin(\frac{P}{2}\pi x)}{P \sin(\frac{1}{2}\pi x)}$ . To generate planar waves aligning with the sub-array channel,  $\beta'_k$  is typically devised according to the spatial direction  $\sin \theta_k$  at the center frequency [29], i.e.,

$$\beta'_k = -\sin \theta_k. \quad (14)$$

By substituting (14) into (13), we obtain

$$\tilde{\mathbf{h}}_m^{(k)T} \mathbf{f}_m^{(k)} = e^{-k_m(r'_k+r_k)} \Xi_P(\epsilon_m \sin \theta_k), \quad (15)$$

where  $\epsilon_m = \eta_m - 1 = \frac{B}{f_c} (\frac{2}{M-1}m - 1)$ . The subsequent objective of our PDF method is to find proper  $\{r'_k\}$  to maximize the beamforming gain on the user location  $(r, \theta)$  over the entire bandwidth. Hence, the corresponding optimization problem can be formulated as

$$\begin{aligned} \max_{\{r'_k\}} & \frac{1}{MK} \sum_{m=1}^M \left| \sum_{k=0}^{K-1} e^{-jk_m(r'_k+r_k)} \Xi_P(\epsilon_m \sin \theta_k) \right| \quad (16) \\ \text{s.t.} & r'_k \geq 0 \quad k \in \{1, 2, \dots, K\}. \end{aligned}$$

We provide the following **Lemma 1** to solve problem (16).

**Lemma 1:** If  $|\epsilon_m| \leq \frac{2}{P}$  for  $\forall m \in \{0, 1, \dots, M-1\}$ , then the optimal solution to problem (16) is

$$r'_k = L - r_k, \quad (17)$$

where  $L$  is a global distance parameter chosen to ensure  $\min\{r'_k\} \geq 0$ .

*Proof:* By substituting (17) into (15), the beamforming gain of the  $k^{\text{th}}$  sub-array can be rewritten as

$$\tilde{\mathbf{h}}_m^{(k)T} \mathbf{f}_m^{(k)} = P e^{-jk_m L} \Xi_P(\epsilon_m \sin \theta_k). \quad (18)$$

The condition  $|\epsilon_m| \leq \frac{2}{P}$  means that the parameters  $|\epsilon_m \sin \theta_k| \leq |\epsilon_m|$  are within the main lobe of  $\Xi_P(\cdot)$  for all subcarriers  $f_m$ . Hence, it is obvious that  $\Xi_P(\epsilon_m \sin \theta_k) > 0$ , and the beamforming gain can be presented as

$$\frac{1}{N} \left| \sum_k \tilde{\mathbf{h}}_m^{(k)T} \mathbf{f}_m^{(k)} \right| = \frac{1}{K} \sum_k \Xi_P(\epsilon_m \sin \theta_k). \quad (19)$$

In addition, according to the Cauchy-Schwarz inequality, the beamforming gain  $G_m$  has an upper bound:

$$G_m \leq \frac{1}{K} \sum_k \left| \tilde{\mathbf{h}}_m^{(k)T} \mathbf{f}_m^{(k)} \right| = \frac{1}{K} \sum_k \Xi_P(\epsilon_m \sin \theta_k). \quad (20)$$

It is clear from (19) and (20) that  $r'_k$  is the optimal solution to maximize  $G_m$  at frequency  $f_m$ . Moreover, since  $r'_k$  is

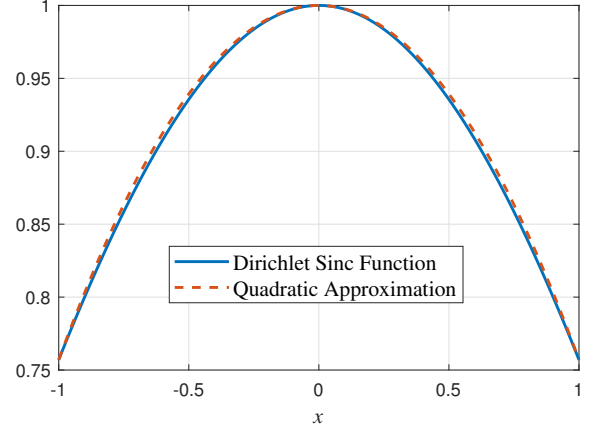


Fig. 5. Quadratic fitting  $1 - \left(1 - \Xi_P(\frac{B}{2f_c})\right) x^2$  of the Dirichlet sinc function  $\Xi_P(\frac{B}{2f_c} x)$ , where  $x \in [-1, 1]$ ,  $P = 32$ ,  $B = 5$  GHz, and  $f_c = 100$  GHz.

frequency independent, it is the optimal solution to all sub-carriers and thus optimal to problem (16), which completes the proof. ■

To sum up, (14) and (17) complete the beamforming design for the proposed PDF method. In the next subsection, theoretical analysis will be provided to validate the efficiency of the proposed PDF method in alleviating the near-field beam split effect.

### C. Analysis of Beamforming Gain Performance

This subsection presents an analysis of the performance of the proposed PDF method for large numbers  $M$  and  $K$ . We begin by introducing **Lemma 2**, which provides the average beamforming gain over all sub-carriers achieved by the PDF method.

**Lemma 2:** Suppose the user is located in the far-field region of each sub-array and  $|\epsilon_m| \leq \frac{2}{P}$  for  $\forall m$ , then the average beamforming gain over all sub-carriers achieved by (11) can be approximated as

$$\frac{1}{M} \sum_{m=0}^{M-1} G_m \approx 1 - \frac{1 - \Xi_P(\frac{B}{2f_c})}{MK} \sum_{m=0}^{M-1} \frac{\epsilon_m^2}{(\frac{B}{2f_c})^2} \sum_{k=0}^{K-1} \sin^2 \theta_k. \quad (21)$$

*Proof:* Plugging (14) and (17) into (13), the average beamforming gain could be expressed as

$$\frac{1}{M} \sum_{m=0}^{M-1} G_m = \frac{1}{MK} \sum_{m=0}^{M-1} \sum_{k=0}^{K-1} \Xi_P(\epsilon_m \sin \theta_k). \quad (22)$$

It is intractable to compute (22) as the variables  $\epsilon_m$  and  $\sin \theta_k$  are included in Dirichlet sinc functions  $\Xi_P(\epsilon_m \sin \theta_k)$ . To deal with this problem, we use a two-variable quadratic function to fit function  $\Xi_P(ab)$ . To be specific, because  $|\epsilon_m| \leq \epsilon_{M-1} = \frac{B}{2f_c}$  and  $|\sin \theta_k| \leq 1$ , the following five points on  $\Xi_P(ab)$  are used for function fitting:  $(0, 0, 1)$ ,  $(\frac{B}{2f_c}, 1, \Xi_P(\frac{B}{2f_c}))$ ,  $(\frac{B}{2f_c}, -1, \Xi_P(\frac{B}{2f_c}))$ ,  $(-\frac{B}{2f_c}, 1, \Xi_P(\frac{B}{2f_c}))$ ,  $(-\frac{B}{2f_c}, -1, \Xi_P(\frac{B}{2f_c}))$ . Therefore, we have

$$\Xi_P(ab) \approx 1 - (1 - \Xi_P(\frac{B}{2f_c})) \frac{a^2}{(\frac{B}{2f_c})^2} b^2. \quad (23)$$

The graph of function  $1 - (1 - \Xi_P(\frac{B}{2f_c}))x^2$  is depicted in Fig. 5 for parameters  $P = 32$ ,  $B = 5$  GHz, and  $f_c = 100$  GHz, which is quite close to the Dirichlet sinc function  $\Xi_P(\frac{B}{2f_c}x)$ . Finally, substituting (23) into (22) and replacing  $(a, b)$  with  $(\epsilon_m, \sin \theta_k)$ , we could arrive at the conclusion (21). ■

**Lemma 2** allows us to separately compute the factors affecting the average beamforming gain: the factor  $\sum_m \frac{\epsilon_m^2}{(\frac{B}{2f_c})^2}$  arising from the wideband effect and the factor  $\sum_k \sin^2 \theta_k$  resulting from the near-field effect.

Specifically, the following **Corollary 1** presents a more analytical form of (21).

**Corollary 1:** For large numbers  $K$  and  $M$ , the average beamforming gain  $G = \frac{1}{M} \sum_{m=0}^{M-1} G_m$  in (21) could be represented as

$$G = \frac{1}{M} \sum_{m=0}^{M-1} G_m \approx 1 - \gamma(B, f_c, P) \times \xi(r, \theta, D), \quad (24)$$

where

$$\gamma(B, f_c, P) = \frac{1 - \Xi_P(\frac{B}{2f_c})}{3}, \quad (25)$$

$$\xi(r, \theta, D) = 1 - \frac{r \cos \theta}{D} \left( \pi \mathbb{I}_{2r \leq D} + \arctan \frac{Dr \cos \theta}{r^2 - \frac{1}{4}D^2} \right). \quad (26)$$

Here,  $D = (KP - 1)d \approx KPd$ ,  $\mathbb{I}_{2r \leq D} = 1$  if  $2r \leq D$ , and  $\mathbb{I}_{2r \leq D} = 0$  otherwise.

*Proof:* The key to this proof lies in calculating the close-form expressions of  $\sum_m \frac{\epsilon_m^2}{(\frac{B}{2f_c})^2}$  and  $\sum \sin^2 \theta_k$ . Firstly, due to the fact that  $1^2 + 2^2 + \dots + n^2 = \frac{n(n+1)(2n+1)}{6}$ , we can represent  $\sum_m \frac{\epsilon_m^2}{(\frac{B}{2f_c})^2}$  as

$$\sum_m \frac{\epsilon_m^2}{(\frac{B}{2f_c})^2} = \sum_{m=0}^{M-1} \left( \frac{2}{M-1}m - 1 \right)^2 = \frac{M(M+1)}{3(M-1)}, \quad (27)$$

Then for a large number  $M$ ,  $\sum_m \frac{\epsilon_m^2}{(\frac{B}{2f_c})^2}$  could be further approximated as  $\frac{M}{3}$ .

As for the second summation  $\sum_k \sin^2 \theta_k$ , it could be rewritten in an integral form for a large number  $K$ :

$$\begin{aligned} \sum_{k=0}^{K-1} \sin^2 \theta_k &= \sum_{k=0}^{K-1} \frac{(r \sin \theta - \delta_K^{(k)} Pd)^2}{r^2 + (\delta_K^{(k)} Pd)^2 - 2\delta_K^{(n)} Pdr \sin \theta} \\ &\approx \int_{-\frac{K}{2}}^{\frac{K}{2}} \frac{(r \sin \theta - kPd)^2}{r^2 + (kPd)^2 - 2kPdr \sin \theta} dk \\ &\stackrel{(a)}{=} K - \frac{r \cos \theta}{Pd} \arctan \frac{Pdk - r \sin \theta}{r \cos \theta} \Big|_{-K/2}^{K/2} \\ &\stackrel{(b)}{=} K - \frac{r \cos \theta}{Pd} \left( \pi \mathbb{I}_{2r \leq D} + \arctan \frac{Dr \cos \theta}{r^2 - \frac{1}{4}D^2} \right). \end{aligned} \quad (28)$$

where  $D = (KP - 1)d \approx KPd$  for large  $KP$ . Here, (a) comes from the indefinite integral  $\int \frac{dx}{A+2Bx+Cx^2} = \frac{1}{\sqrt{AC-B^2}} \arctan \frac{Cx+B}{\sqrt{AC-B^2}}$  for  $AC > B^2$  [30], and (b) arises from a characteristic of the inverse tangent function:

$$\arctan A + \arctan B = \begin{cases} \arctan \frac{A+B}{1-AB} & (AB < 1) \\ \pi + \arctan \frac{A+B}{1-AB} & (AB > 1) \end{cases}$$

for  $A > 0$ . Finally, by combining (21), (27), and (28), the conclusion of **Corollary 1** could be obtained. ■

**Corollary 1** yields several crucial conclusions. The beamforming gain loss of our PDF method arises from two factors: the loss caused by wideband effect  $\gamma(B, f_c, P)$  and the loss posed by the geometry  $\xi(r, \theta, D)$ .

First, the geometry loss  $\xi(r, \theta, D)$  captures the degree of beam split effect with varying user locations. Due to the non-decreasing property of function  $\arctan(\cdot)$ , it is straightforward to prove that  $\xi(r, \theta, D)$  monotonically increases w.r.t  $|\theta|$  when  $r > \frac{1}{2}D$ . This fact implies that a larger angle of arrival leads to a more significant beamforming gain loss caused by near-field beam split, making it harder for our PDF method to compensate for this loss. Similar conclusions also appear in existing far-field beam split solutions. Moreover,  $\xi(r, \theta, D)$  could account for the geometry loss in both far-field and near-field regions, as it incorporates the distance parameter  $r$ . A simple evidence is that when  $r \rightarrow +\infty$ ,  $\xi(r, \theta, D)$  tends to  $\sin^2 \theta$ , which is exactly the geometry loss in far-field conditions provided in [21].

Second,  $\gamma(B, f_c, P)$  is induced by the loss of beam split within each sub-array. This is due to the employment of PS based frequency-independent beamforming for each sub-array. Fortunately, since the number  $P$  of a sub-array's antennas is much less than the number  $N$  of the entire array's antennas, this loss  $\gamma(B, f_c, P)$  can approach 0 by choosing an appropriate value of  $P$ . To be specific, it can be easily proven that  $\gamma(B, f_c, P)$  is an increasing function w.r.t  $P$  when  $P \leq \frac{4f_c}{B}$ . With a smaller  $P$ , the impact of intra-array beam split is reduced. For instance, when  $P = 32$ ,  $B = 5$  GHz,  $f_c = 100$  GHz,  $r = 10$  m,  $D = 0.5$  m, and  $\theta = \frac{\pi}{3}$ , we have  $\gamma(B, f_c, P) \approx 0.081$ ,  $\xi(r, \theta, D) \approx 0.7496$ , and  $1 - \gamma(B, f_c, P) \times \xi(r, \theta, D) \approx 0.9393$ . This implies that more than 93% average beamforming gain is achievable by the proposed PDF method.

#### D. Extension to Multi-User Hybrid Beamforming

In this section, we extend the proposed PDF method to multi-user hybrid beamforming systems in Section II. The same DPP architecture depicted in Fig. 4 is employed for each RF chain. Specifically, recall that the introduction of TTD circuits makes the analog beamformer frequency-dependent. Therefore, we denote this new analog beamformer as  $\mathbf{F}_m = [\mathbf{f}_{0,m}, \mathbf{f}_{1,m}, \dots, \mathbf{f}_{U-1,m}]$ , where each  $\mathbf{f}_{u,m}$  satisfies the circuit restriction of DPP:

$$\begin{cases} \mathbf{f}_{u,m} = [\mathbf{f}_{u,m}^{(0)T}, \mathbf{f}_{u,m}^{(1)T}, \dots, \mathbf{f}_{u,m}^{(K-1)T}]^T, \\ \mathbf{f}_{u,m}^{(k)} = \frac{e^{-jk_m r'_{u,k}}}{\sqrt{N}} [e^{j\pi \delta_P^{(0)} \beta'_{u,k}}, \dots, e^{j\pi \delta_P^{(P-1)} \beta'_{u,k}}]^T. \end{cases} \quad (29)$$

There,  $r'_{u,k}$  and  $\beta'_{u,k}$  refer to the adjustable distance parameter of the  $k^{\text{th}}$  TTD element and the adjustable phase shift parameter of the  $k^{\text{th}}$  sub-array connected to  $u^{\text{th}}$  RF chain, respectively. The basic idea of PDF algorithm is to align  $\mathbf{f}_{u,m}$  with  $\mathbf{h}_{u,m}$  user-by-user in the analog domain and eliminate the inter-user interference by the digital precoder. A step-by-step algorithm procedure is summarized in **Algorithm 1**.



---

**Algorithm 1:** The proposed PDF algorithm
 

---

**Require:**

Channel matrix  $\mathbf{H}_m$ ; the user locations  $\{(r_u, \theta_u)\}_{u=0}^{U-1}$ ; the total transmit power  $\rho$

**Ensure:**

The digital beamformer  $\mathbf{D}_m$  and the analog beamformer  $\mathbf{F}_m$

- 1: **for**  $u \in \{0, 1, \dots, U-1\}$  **do**
  - 2:   **for**  $k \in \{0, 1, \dots, K-1\}$  **do**
  - 3:     Determine the distance parameter of the  $k^{\text{th}}$  TTD element:  $r'_{u,k} \leftarrow -r_{u,k} = -\sqrt{r_u^2 + (\delta_K^{(k)} Pd)^2 - 2\delta_K^{(k)} Pdr_u \sin \theta_u}$
  - 4:     Determine the phase shift of the  $k^{\text{th}}$  sub-array:  $\beta'_{u,k} \leftarrow -\sin \theta_{u,k} = -\frac{r_u \sin \theta_u - \delta_K^{(k)} Pd}{\sqrt{r_u^2 + (\delta_K^{(k)} Pd)^2 - 2\delta_K^{(k)} Pdr_u \sin \theta_u}}$
  - 5:     Shift  $r'_{u,k}$  by  $L = \min_k \{r'_{u,k}\}$  to make them positive:  $r'_{u,k} \leftarrow L + r'_{u,k}$
  - 6:   **end for**
  - 7:   Build the beamforming vector connected to the  $u^{\text{th}}$  RF chain using (29)
  - 8: **end for**
  - 9: Build the analog beamformer:  $\mathbf{F}_m \leftarrow [\mathbf{f}_{0,m}, \mathbf{f}_{1,m}, \dots, \mathbf{f}_{U-1,m}]$
  - 10: Calculate the digital beamformer by ZF:  $\mathbf{D}_m \leftarrow \mathbf{F}_m^H \mathbf{H}_m^H (\mathbf{H}_m \mathbf{F}_m \mathbf{F}_m^H \mathbf{H}_m^H)^{-1}$
  - 11: Normalize the digital beamformer to power  $\rho$ :  $\mathbf{D}_m \leftarrow \frac{\sqrt{\rho} \mathbf{D}_m}{\|\mathbf{F}_m \mathbf{D}_m\|_F}$
  - 12: **return**  $\mathbf{F}_m$  and  $\mathbf{D}_m$ .
- 

Specifically, the analog beamformer is first determined in steps 1 ~ 9. According to (14) and (17), to align the  $u^{\text{th}}$  beamforming vector  $\mathbf{f}_{u,m}$  with the  $u^{\text{th}}$  user,  $r'_{u,k}$  and  $\beta'_{u,k}$  are determined by  $-r_{u,k}$  and  $-\sin \theta_{u,k}$ , respectively. Here,  $r_{u,k} = \sqrt{r_u^2 + (\delta_K^{(k)} Pd)^2 - 2\delta_K^{(k)} Pdr_u \sin \theta_u}$  and  $\beta'_{u,k} = -\sin \theta_{u,k} = -\frac{y_u - \delta_K^{(k)} Pd}{r_{u,k}} = -\frac{r_u \sin \theta_u - \delta_K^{(k)} Pd}{\sqrt{r_u^2 + (\delta_K^{(k)} Pd)^2 - 2\delta_K^{(k)} Pdr_u \sin \theta_u}}$ , which leads to steps 3 ~ 4. Then, according to **Lemma 1**,  $L = \min_k \{r'_{u,k}\}$  can be used to shift the distance parameters to make sure  $r'_{u,k} \geq 0$ , which is reflected in step 5. Last, the analog beamformer  $\mathbf{F}_m$  per sub-carrier is constructed one-by-one in step 9. As for the digital precoder  $\mathbf{D}_m$ , it is built on the zero-forcing (ZF) rule to eliminate inter-user interference. Besides, the power of  $\mathbf{D}_m$  is normalized to  $\rho$  to guarantee the power constraint per subcarrier, which completes the PDF algorithm.

#### IV. EFFECTIVE RAYLEIGH DISTANCE

In the previous section, we assume that the user is positioned within the near-field range of the entire array while being in the far-field range of each sub-array. Therefore, it is essential to accurately identify the near-field ranges of a sub-array and the entire array. Traditionally, the classical Rayleigh distance is employed as a standard for quantifying the near-field range. However, our experiments show that the Rayleigh distance overestimates the actual near-field range. For example, when the array aperture is  $D = 0.384$  m and the carrier is  $f_c = 100$  GHz, the Rayleigh distance is around 98 m. Yet, the far-field wideband beamforming method [21] only exhibits a noticeable beamforming gain loss when the distance is less than 30 m. This fact implies that classical Rayleigh distance overestimates the near-field range when evaluating channel capacity. This result is attributed to the fact that classical Rayleigh distance is derived by evaluating the largest phase error between planar wave and spherical wave, which does not directly affect the transmission rate. By contrast, the near-field effect has a directly impact on beamforming gain, which in turn plays a

pivotal role in determining transmission rates. Therefore, it becomes apparent that a more precise metric for defining the near-field range in terms of beamforming gain is required.

Specifically, we first introduce the derivation of the classical Rayleigh distance by the evaluation of phase error. For ease of discussion, we only consider an arbitrary frequency  $f_m$  and an arbitrary user. Therefore, the subscript  $m$  and  $u$  is omitted in this section. Denote  $\mathbf{h}(r, \theta)$  as the near-field channel as a function of user location  $(r, \theta)$ , of which the  $n^{\text{th}}$  entry is given by  $[\mathbf{h}(r, \theta)]_n = ge^{-jkr^{(n)}} = ge^{-jk(r^2 + (\delta_N^{(n)} d)^2 - 2\delta_N^{(n)} dr \sin \theta)^{1/2}}$ , where  $g$  denotes the path loss and  $k = \frac{2\pi f}{c}$  is the wavenumber. By utilizing the far-field approximation in (5), the far-field channel is expressed as  $[\mathbf{h}_{\text{far}}(r, \theta)]_n = [\mathbf{h}(+\infty, \theta)]_n = ge^{-jk(r - \delta_N^{(n)} d \sin \theta)}$ . Consequently, the phase error between  $[\mathbf{h}(r, \theta, f_c)]_n$  and  $[\mathbf{h}_{\text{far}}(r, \theta, f_c)]_n$  is defined as

$$\begin{aligned} E_n(r, \theta) &= |\angle[\mathbf{h}(r, \theta)]_n - \angle[\mathbf{h}_{\text{far}}(r, \theta)]_n| \\ &= |kr^{(n)} - k(r - \delta_N^{(n)} d \sin \theta)|. \end{aligned} \quad (30)$$

Subsequently, the definition of Rayleigh distance is as follows [13]: if the distance  $r$  from user to BS exceeds the Rayleigh distance  $R$ , then the largest phase error  $E(r) = \max_{n, \theta} E_n(r, \theta)$  is no more than  $\frac{\pi}{8}$ . That is to say, once the largest phase error  $E(r)$  surpasses  $\frac{\pi}{8}$ , the user is situated in the near-field region. To derive the close-form expression of  $E(r)$ , the second-order Taylor expansion  $(1+x)^{\frac{1}{2}} \approx 1 + \frac{1}{2}x - \frac{1}{8}x^2$  is commonly used [31] to approximate the distance  $r^{(n)}$  as

$$\begin{aligned} r^{(n)} &= \sqrt{r^2 - 2r\delta_N^{(n)} d \sin \theta + (\delta_N^{(n)} d)^2} \\ &\approx r - \delta_N^{(n)} d \sin \theta + \frac{(\delta_N^{(n)} d)^2 \cos^2 \theta}{2r}. \end{aligned} \quad (31)$$

In the field of microwave and antenna, the approximation (31) is known as the Fresnel approximation [24]. Next, the phase error can be approximated as  $E_n(r, \theta) \approx k_c \frac{(\delta_N^{(n)} d)^2 \cos^2 \theta}{2r}$ .

Given that  $\cos^2 \theta \leq 1$  and  $\delta_N^{(n)} = n - \frac{N-1}{2}$ , we have

$$E(r) = \max_{n, \theta} E_n(r, \theta) \approx k \frac{(0.5(N-1)d)^2}{2r} = \frac{D^2 \pi}{4r\lambda}. \quad (32)$$

In order for  $E(r) \leq \frac{\pi}{8}$ , it is necessary to make  $r \geq \frac{2D^2}{\lambda}$ . Consequently, the Rayleigh distance is given by

$$R \approx \frac{2D^2}{\lambda}. \quad (33)$$

On the other hand, we define a new effective Rayleigh distance via the evaluation of beamforming gain loss. To elaborate, the normalized coherence between the channel  $\mathbf{h}(r, \theta)$  and its far-field approximation  $\mathbf{h}_{\text{far}}(r, \theta)$  is characterized by

$$\mu(r, \theta) = \frac{1}{|g|^2 N} |\mathbf{h}^H(r, \theta) \mathbf{h}_{\text{far}}(r, \theta)|. \quad (34)$$

The coherence  $\mu(r, \theta)$  equivalents to the achievable beamforming gain at frequency  $f$  when the BS utilizes the far-field beamforming vector  $\mathbf{f} = \frac{1}{|g|\sqrt{N}} \mathbf{h}_{\text{far}}^*(r, \theta)$  to serve a user located at  $(r, \theta)$ . Clearly, this beamforming gain would gradually decline when the user is moving close to BS and the near-field effect becomes remarkable. When the beamforming gain loss, denoted as  $1 - \mu(r, \theta)$ , exceeds a predefined threshold  $\Delta$ , it indicates that the user has entered the near-field region. Consequently, the boundary  $R_{\text{eff}}$ , where  $1 - \mu(R_{\text{eff}}, \theta)$  exactly equals to  $\Delta$ , is defined as the effective Rayleigh distance. Notably, the direct influence of beamforming gain  $\mu(r, \theta)$  on the received signal power makes  $R_{\text{eff}}$  a more accurate metric for characterizing the near-field range in communication systems. **Lemma 3** gives out the close-form expression of effective Rayleigh distance  $R_{\text{eff}}$ .

**Lemma 3:** We define the effective Rayleigh distance  $R_{\text{eff}}$  such that the inequality  $1 - \mu(r, \theta) \geq \Delta$  always holds for  $0 < r \leq R_{\text{eff}}$ . Then, the value of  $R_{\text{eff}}$  is given by

$$R_{\text{eff}} \approx C_{\Delta} \cos^2 \theta \frac{2D^2}{\lambda}, \quad (35)$$

where  $C_{\Delta} = \frac{1}{4\beta_{\Delta}^2}$  and  $\beta_{\Delta}$  is the solution of the equation  $\frac{1}{\beta_{\Delta}} \left| \int_0^{\beta_{\Delta}} e^{-j\frac{1}{2}\pi t^2} dt \right| = \Delta$ .

*Proof:* To obtain the value of the effective Rayleigh distance, we need to derive the close-form expression of  $\mu(r, \theta)$ . Based on the second-order Taylor expansion in (31),  $\mu(r, \theta)$  can be expressed as

$$\begin{aligned} \mu(r, \theta) &\approx \frac{1}{N} \left| \sum_{n=0}^{N-1} e^{-j\pi \frac{(\delta_N^{(n)} d)^2 \cos^2 \theta}{\lambda r}} \right| \\ &= \frac{1}{N} \left| \sum_{m=-\frac{1}{2} + \frac{1}{2N}}^{\frac{1}{2} - \frac{1}{2N}} e^{-j\pi \frac{m^2 (Nd)^2 \cos^2 \theta}{\lambda r}} \right|. \end{aligned} \quad (36)$$

Notice that the operator  $\sum_{m=-\frac{1}{2} + \frac{1}{2N}}^{\frac{1}{2} - \frac{1}{2N}}$  performs the summation over  $m = -\frac{1}{2} + \frac{1}{2N}, -\frac{1}{2} + \frac{3}{2N}, -\frac{1}{2} + \frac{5}{2N}, \dots, \frac{1}{2} - \frac{1}{2N}$ . Let's define  $\zeta = \frac{N^2 d^2 \cos^2 \theta}{\lambda r}$  for brevity. Since the number of antennas  $N$  is quite large, (36) can be represented in an integral form as

$$\mu(r, \theta) = \left| \int_{-1/2}^{1/2} e^{-j\pi m^2 \zeta} dm \right| = 2 \left| \int_0^{1/2} e^{-j\pi m^2 \zeta} dm \right|. \quad (37)$$

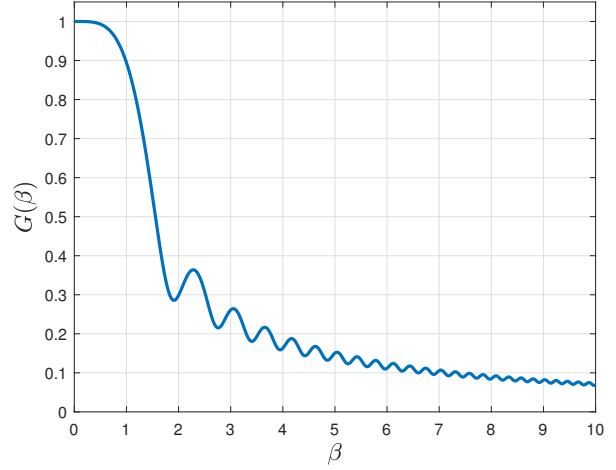


Fig. 6. The numerical results of  $G(\beta)$

Additionally, we introduce the variable transformation:  $\frac{1}{2}t^2 = m^2\zeta$ . Then,  $\mu(r, \theta)$  can be rewritten as

$$\mu(r, \theta) = \frac{2}{\sqrt{2\zeta}} \left| \int_0^{\frac{\sqrt{2\zeta}}{2}} e^{-j\frac{1}{2}\pi t^2} dt \right| = G(\beta), \quad (38)$$

where  $G(\beta) = \left| \int_0^{\beta} e^{-j\frac{1}{2}\pi t^2} dt \right| / \beta$  and  $\beta = \frac{\sqrt{2\zeta}}{2} = \sqrt{\frac{N^2 d^2 \cos^2 \theta}{2\lambda r}} = \sqrt{\frac{D^2 \cos^2 \theta}{2\lambda r}}$ . It is clear from (38) that the coherence heavily relies on the characteristics of the function  $G(\beta)$ . Fortunately,  $G(\beta)$  does not contain any parameters, allowing us to obtain its numerical result via offline integration.

As illustrated in Fig. 6, the function  $G(\beta)$  shows a significant downward trend w.r.t  $\beta^3$ . Therefore, to make the beamforming gain loss  $1 - \mu(r, \theta) = 1 - G(\beta)$  larger than the threshold  $\Delta$ , we need  $\beta \geq \beta_{\Delta}$ , where  $G(\beta_{\Delta}) = 1 - \Delta$ .

In the end, due to the relationship  $\beta = \sqrt{\frac{D^2 \cos^2 \theta}{2\lambda r}}$ , the near-field region is determined by  $r < \frac{1}{4\beta_{\Delta}^2} \cos^2 \theta \frac{2D^2}{\lambda}$ , giving rise to the result  $R_{\text{eff}} = \frac{1}{4\beta_{\Delta}^2} \cos^2 \theta \frac{2D^2}{\lambda}$ . ■

**Lemma 3** offers a comprehensive approach to compute  $R_{\text{eff}}$ . To illustrate, let's consider a simple example where  $\Delta = 5\%$ . We could solve the equation  $\frac{1}{\beta_{\Delta}} \left| \int_0^{\beta_{\Delta}} e^{-j\frac{1}{2}\pi t^2} dt \right| = 0.05$  via the Newton method and obtain  $\beta_{\Delta} = 0.8257$ . Hence, the effective Rayleigh distance is evaluated as  $R_{\text{eff}} = 0.367 \cos^2 \theta \frac{2D^2}{\lambda}$ .

It is evident from (33) and (35) that effective Rayleigh distance needs two more variables compared to Rayleigh distance, i.e., the constant  $C_{\Delta}$  related to beamforming gain loss and the angle of arrival  $\theta$ . These two variables enable effective Rayleigh distance to accurately capture where far-field beamforming are not applicable, and thus make it a more accurate metric for quantifying near-field region. In Section V, the accuracy of effective Rayleigh distance will be verified through simulation.

<sup>3</sup>The function  $G(\beta)$  is applied in our another paper [32] as well to evaluate the quasi-orthogonality of near-field channels, while  $G(\beta)$  is used to derive the effective Rayleigh distance in this paper.

### A. Discussion on the Fresnel Approximation

In deriving the effective Rayleigh distance, the Fresnel approximation (31) is employed. As indicated in [13], the approximation (31) is accurate when the distance  $r$  is larger than the ‘‘Fresnel distance’’  $0.5\sqrt{\frac{D^3}{\lambda_c}}$ . To validate the rationality of the Fresnel approximation, we would like to show that the effective Rayleigh distance  $0.367 \cos^2 \theta \frac{2D^2}{\lambda_c}$ , with  $\Delta = 5\%$ , is much larger than the Fresnel distance. Take it into account that the section range of a typical cell is around  $\frac{2\pi}{3}$ , thus  $\theta$  is restricted between  $-\frac{\pi}{3}$  and  $\frac{\pi}{3}$ . Accordingly,  $0.367 \cos^2 \theta \frac{2D^2}{\lambda_c} \geq 0.5\sqrt{\frac{D^3}{\lambda_c}}$  is equivalent to  $N > 15.8490$ . Given that an extremely large antenna array have hundreds or thousands of antennas, which is greatly larger than 15.8490, the effective Rayleigh distance is much longer than the Fresnel distance, resulting in the accuracy of approximation (31).

### B. Discussion on the Piecewise-Far-Field Approximation

The effective Rayleigh distance is capable of verifying the accuracy of the piecewise-far-field approximation as well. Recall that the user should locate in the far-field region of each sub-array, i.e.,  $r_k$  must be larger than  $0.367 \cos^2 \theta_k \frac{2(P-1)^2 d^2}{\lambda_c}$  with  $\Delta = 5\%$ . Take a small sub-array configuration as an example:  $P = 32$  and  $f_c = 100$  GHz. The effective Rayleigh distance per sub-array is upper bounded by  $0.367 \cos^2 \theta_k \frac{2(P-1)^2 d^2}{\lambda_c} \leq 0.367 \frac{2(P-1)^2 d^2}{\lambda_c} = 0.5286\text{m}$ . In this context, as long as the user-to-sub-array distance  $r_k$  is larger than 0.5286m, a common situation in mobile communications, each sub-array’s channel can be precisely modeled as far-field. Therefore, under a small sub-array configuration, the piecewise-far-field approximation is accurate.

### C. Discussion on the Number of Antennas per Sub-Array

In this sub-section, by combining **Lemma 1**, **Lemma 2**, and **Lemma 3**, the value of the essential parameter  $P$ , the number of antennas per sub-array, is designed.

The value of  $P$  needs to meet three key requirements. First, as stated in **Lemma 1**,  $|\epsilon_m| \leq \frac{2}{P}$  holds for  $\forall m$ . Owing to the fact that  $\max |\epsilon_m| = \frac{B}{2f_c}$ , we have  $P \leq \frac{4f_c}{B}$ .

Next, we made an assumption that the user is located in the far-field region of each sub-array. We evaluate the effective Rayleigh distance at the center frequency  $f_c$  with a wavelength  $\lambda_c$ . Suppose the user’s activity range is  $r \in [\rho_l, \rho_h]$  and  $\theta \in [-\theta_h, \theta_h]$ , where  $\rho_l$  and  $\rho_h$  can be regarded as the least allowable distance from user to BS and the cell radius, and  $\theta_h$  refers to the sector range of a cell. Applying **Lemma 3**, the effective Rayleigh distance of a sub-array is  $C_\Delta \cos^2 \theta \frac{2(Pd)^2}{\lambda_c} = \frac{1}{2} C_\Delta \cos^2 \theta P^2 \lambda_c \leq \frac{1}{2} C_\Delta P^2 \cos^2 \theta_h \lambda_c^2$ . Then, to keep the user consistently outside the region bounded by  $\frac{1}{2} C_\Delta \cos^2 \theta P^2 \lambda_c$ , we can let  $\rho_l \geq \frac{1}{2} C_\Delta \cos^2 \theta_h P^2 \lambda_c$  and arrive at the condition  $P \leq \sqrt{\frac{2\rho_l}{C_\Delta \cos^2 \theta_h \lambda_c}}$ .

Finally, in order to guarantee the performance of PDF method, we would like to design  $P$  such that the least average

TABLE I: System Configurations

The number of the BS antennas $N$	256
The number of Users $U$	1, 4
The center frequency $f_c$	100 GHz
The bandwidth $B$	5 GHz
The number of subcarriers $M$	256
The user’s activity range $[\rho_l, \rho_h]$	[1 m, 100 m]
The sector range of a cell $\theta_h$	$\pi/3$
Threshold parameter $\Delta$	5%
Threshold parameter $\delta$	90%
The number of a sub-array’s antennas $P$	32
The number of TTDs $K$	8

beamforming gain in **Corollary 1** is greater than a predefined threshold  $\delta$ . This requirement can be formulated as follows:

$$\begin{aligned} \min_{r, \theta} G &= 1 - \gamma(B, f_c, P) \max_{r, \theta} \xi(r, \theta, D) \geq \delta. \\ \Rightarrow \Xi_P\left(\frac{B}{2f_c}\right) &\geq 1 - \frac{3(1-\delta)}{\max_{r, \theta} \xi(r, \theta, D)} \end{aligned} \quad (39)$$

Notice that  $\max_{r, \theta} \xi(r, \theta, D) = \max_r \xi(r, \theta_h, D)$  given that  $\xi(r, \theta, D)$  is a decreasing function w.r.t  $|\theta|$ . Furthermore, we can utilize the gradient ascend method to solve  $\max_r \xi(r, \theta_h, D)$ , and thereafter employ the Newton method to attain  $P_\delta$  from the equation  $\Xi_{P_\delta}\left(\frac{B}{2f_c}\right) = 1 - \frac{3(1-\delta)}{\max_r \xi(r, \theta_h, D)}$ . Finally, taking it into consideration the monotonic decreasing property of function  $\Xi_P\left(\frac{B}{2f_c}\right)$  w.r.t  $P$ , we can draw the conclusion  $P \leq P_\delta$ .

As a result, applying the three requirements above, the number of antennas per sub-array  $P$  should satisfy

$$P \leq \min \left\{ \frac{4f_c}{B}, \sqrt{\frac{2\rho_l}{C_\Delta \cos^2 \theta_h \lambda_c}}, P_\delta \right\}. \quad (40)$$

For instance, considering the following parameters:  $N = 400$ ,  $B = 5$  GHz,  $f_c = 100$  GHz,  $\rho_l = 1$  m,  $\theta_h = \frac{\pi}{3}$ ,  $\Delta = 5\%$ , and  $\delta = 90\%$ , we have  $\frac{4f_c}{B} = 80$ ,  $\sqrt{\frac{2\rho_l}{C_\Delta \cos^2 \theta_h \lambda_c}} \approx 43$  and  $P_\delta \approx 42$ . Therefore, the number of antennas per sub-array can be  $P = 40$ , meaning that a 400-antenna array just needs  $K = \frac{400}{40} = 10$  TTDs to alleviate the near-field beam split effect. Moreover, the lower bound of  $P$  is exactly 1, because a reduced  $P$  leads to an increased deployment of TTD units, enabling the PDF method to achieve more flexible frequency-dependent beamforming. In this context, the beamforming gain is increasingly improved with the reduction of  $P$ .

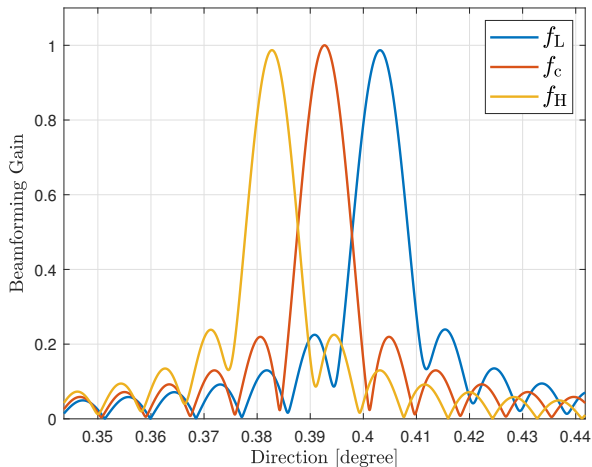
## V. SIMULATION RESULTS

In this section, numerical results are provided to demonstrate the performance of the proposed PDF method and the accuracy of effective Rayleigh distance. The default simulation parameters are presented in Table I unless particularly specified.

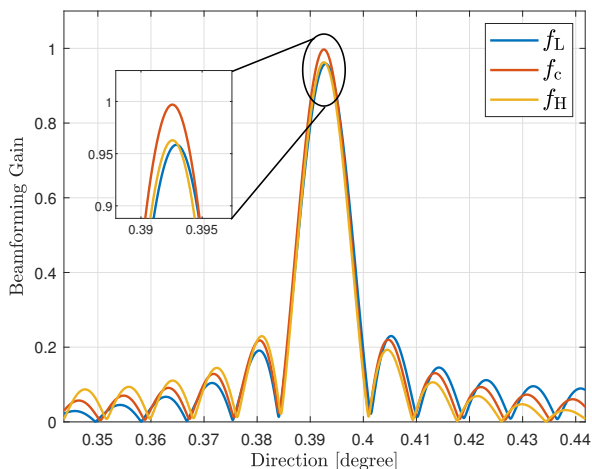
### A. Beamforming Gain

We begin with comparing the beamforming gain performance for single-user scenarios, i.e.,  $U = 1$ .

Fig. 7 presents the beamforming gain performance for different sub-carriers as a function of direction. Here, the user is located at  $(r, \theta) = (2 \text{ m}, \frac{\pi}{8})$ , and we evaluate the



(a) Traditional narrowband beamfocusing [23]

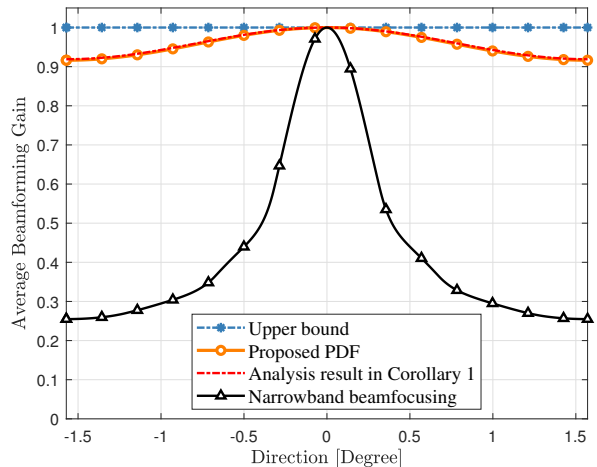
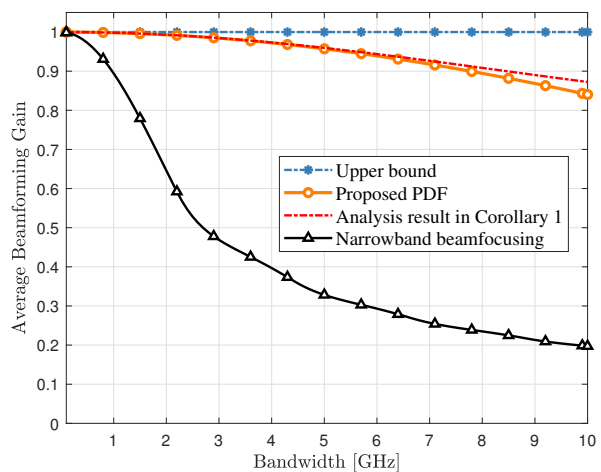


(b) Proposed PDF method

Fig. 7. Beamforming gain per sub-carrier w.r.t direction.

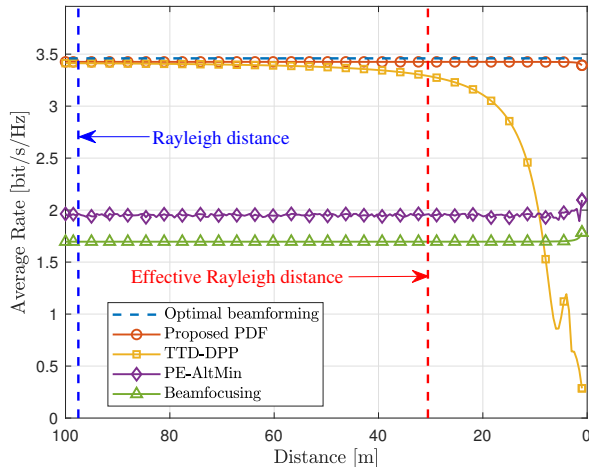
beamforming gain for various frequencies and physical directions. Fig. 7(a) showcases the beamforming gain achieved by traditional near-field narrowband beamfocusing method [23], while Fig. 7(b) presents the results of the proposed PDF method. Let  $f_L$ ,  $f_c$ , and  $f_H$  be the lowest, the center, and the highest frequency, respectively. For the traditional narrowband beamfocusing method, the near-field beam split effect causes the beams at  $f_L$ ,  $f_c$ , and  $f_H$  to be focused on different locations, leading to a significant beamforming gain loss at  $f_L$  and  $f_H$ . However, as illustrated in Fig. 7 (b), the proposed PDF method can effectively focus the energy of the beams at  $f_L$ ,  $f_c$ , and  $f_H$  on the desired user location. Besides, more than 95% beamforming gain on the user location is achieved for  $f_L$  and  $f_H$ . Therefore, the proposed PDF method is able to effectively mitigate the near-field beam split effect.

Fig. 8 illustrates the average beamforming gain performance w.r.t direction  $\theta$ . In this context, the distance  $r$  is fixed as 10 m and the direction  $\theta$  spans from  $-\theta_h$  to  $\theta_h$ . We can observe that the analysis result (24) for average beamforming

Fig. 8. Average beamforming gain w.r.t direction  $\theta$ .Fig. 9. Average beamforming gain performance w.r.t bandwidth  $B$ .

gain is quite close to the real average beamforming gain achieved by the PDF method. With the increment of  $|\theta|$ , the average beamforming gain achieved by both the PDF method and the narrowband beamfocusing method declines. This is attributed to the fact that the beam split effect becomes more significant with larger  $|\theta|$ . Nevertheless, our PDF method could remain more than  $\delta = 90\%$  average beamforming gain over  $\theta \in [-\theta_h, \theta_h]$ , which is consistent with our discussion on the number of a sub-array's numbers in section IV-C.

Moreover, Fig. 9 shows the average beamforming gain performance w.r.t bandwidth  $B$ . In this simulation, the user is located at  $(r, \theta) = (10 \text{ m}, \frac{\pi}{4})$ , and the bandwidth increases from 100 MHz to 10 GHz. It is clear from Fig. 9 that our PDF method could remarkably enhance the near-field beamforming capability by offering near optimal average beamforming gain. For instance, when  $B = 5$  GHz, around 3 times higher average beamforming gain is reaped by the PDF method than narrowband beamfocusing. Besides, it is notable that when the bandwidth is around 10 GHz, our analysis results slightly differ from the real performance of PDF. This is because, with larger bandwidth  $B$ , the precision of quadratic fitting in (23)

Fig. 10. Spectral efficiency w.r.t distance  $r$ .

gets reduced, leading to an error of the analytical beamforming gain.

### B. Spectral Efficiency

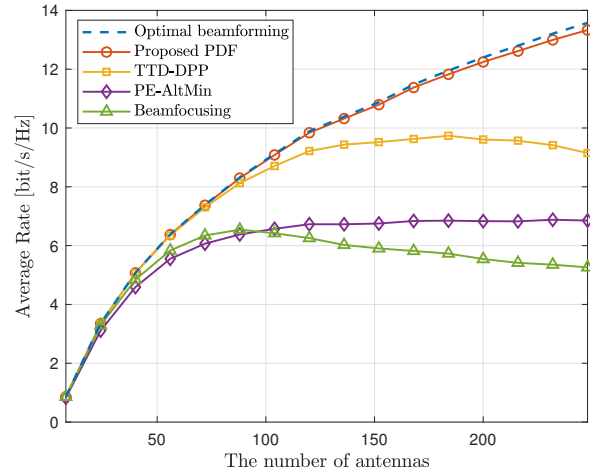
In this subsection, the spectral efficiency, formulated as

$$\text{SE} = \frac{1}{M} \sum_{m=0}^{M-1} \sum_{u=0}^{U-1} \log_2 \left( 1 + \frac{|\mathbf{h}_{u,m}^T \mathbf{F}_m \mathbf{d}_{u,m}|^2}{\sum_{v \neq u} |\mathbf{h}_{u,m}^T \mathbf{F}_m \mathbf{d}_{v,m}|^2 + \sigma^2} \right) \quad (41)$$

is evaluated to compare different beamforming algorithms, where  $\mathbf{d}_{u,m}$  represents the  $u^{\text{th}}$  column of  $\mathbf{D}_{u,m}$ . The path gains  $g_m$  are generated from the Complex Gaussian distribution  $\mathcal{CN}(0, 1)$ . The signal-to-noise ratio (SNR) is defined as  $\text{SNR} = \frac{\rho}{\sigma^2}$ .

The compared algorithms include the narrowband beamforming method in [23], the PE-AltMin algorithm for wideband hybrid beamforming designed in [19], and the TTD-DPP algorithm tailored for solving far-field beam split in [21]. Last, the optimal beamforming achieved by fully TTD arrays, where all phase shifters in Fig. 1 are replaced with TTD circuits and  $\mathbf{f}_{u,m}$  is constructed as  $\mathbf{a}_m^*(r_u, \theta_u)$  in Algorithm 1, is employed as the performance upper bound.

To begin with, the spectral efficiency w.r.t the distance  $r$  is depicted in Fig. 10. The number of users is set as  $U = 1$ . To explicitly illustrate the impact of the near-field effect, we keep the SNR as 10 dB for different distances, where the large-scale fading is compensated by transmit power control. The user moves from  $(\rho_h, \frac{\pi}{8})$  to  $(\rho_l, \frac{\pi}{8})$  in a straight line. We can observe from Fig. 10 that our PDF method outperforms all compared beamforming methods over all distances, and approaches the optimal beamforming. This is attributed to the fact that our PDF method can tackle the near-field effect and beam split effect simultaneously. Moreover, notice that with 256 antennas at  $f_c = 100$  GHz, the classical Rayleigh distance is around 98 meters. However, as illustrated in Fig. 10, the far-field beamforming algorithm TTD-DPP [21] does not exhibit a notable rate loss until the distance is less than 30 meters, which implies that the Rayleigh distance overestimates the

Fig. 11. Spectral efficiency w.r.t the number of antennas  $N$ .

near-field range when evaluating the communication rate. This is attributed to the definition of Rayleigh distance from the phase error [13], which has no direct influence on the spectral efficiency. In contrast, since the beamforming gain makes a direct influence to the received signal power, our newly defined effective Rayleigh distance (35) is a more accurate metric to quantify the near-field range for communications. Specifically, with  $\theta = \pi/8$ ,  $N = 256$ ,  $f_c = 100$  GHz, and  $\Delta = 5\%$ , we have  $R_{\text{eff}} \approx 31$  m. As shown in Fig. 10, the spectral efficiency achieved by the far-field method TTD-DPP starts declining exactly when the distance is less than  $R_{\text{eff}}$ , which demonstrates the accuracy of effective Rayleigh distance.

Fig. 11 evaluates the spectral efficiency w.r.t the number of BS antennas  $N$  ranging from 8 to 256. The other configuration is set as follows:  $U = 4$ ;  $K = 8$ ;  $\text{SNR} = 10$  dB; the distances  $\{r_u\}_{u=0}^{U-1}$  and directions  $\{\theta_u\}_{u=0}^{U-1}$  are sampled from the uniform distribution  $\mathcal{U}(1 \text{ m}, 30 \text{ m})$  and  $\mathcal{U}(-\frac{\pi}{3}, \frac{\pi}{3})$ , respectively. The spectral efficiency are obtained through 10000 times Monte-Carlo simulations. To elaborate, Fig. 11 can be divided into three regions according to the number of BS antennas. When  $N < 50$ , the array aperture is small, so the user is located in the far-field area and the beam split effect is negligible. In this context, all algorithms could achieve good performance. Next, when  $50 < N < 100$ , the far-field beam split effect appears, leading to a severe degradation to the narrowband beamfocusing and PE-AltMin methods. On the other hand, since TTD-DPP and PDF can effectively alleviate far-field beam split, both of them could remain near-optimal average rate performance. Finally, when the number of BS antennas is further increased such that  $N > 100$ , the array aperture is quite large so that the near-field beam split effect is observed. In this context, the TTD-DPP method tailored for far-field beam split is not applicable any more, while the proposed PDF method can remain a stable beamforming performance by mitigating the near-field beam split.

The influence of SNR on the spectral efficiency is investigated in Fig. 12, where the SNR increases from -5 dB to 10 dB. The other settings are as follows:  $U = 4$ ;  $r_u \sim \mathcal{U}(1 \text{ m}, 30 \text{ m})$ ;  $\theta_u \sim \mathcal{U}(-\frac{\pi}{3}, \frac{\pi}{3})$ . The spectral efficiency

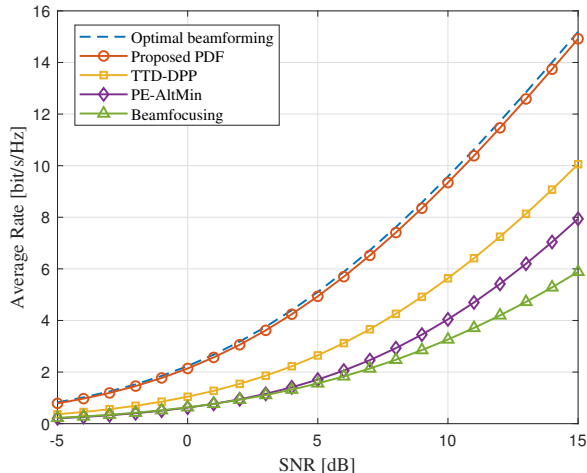
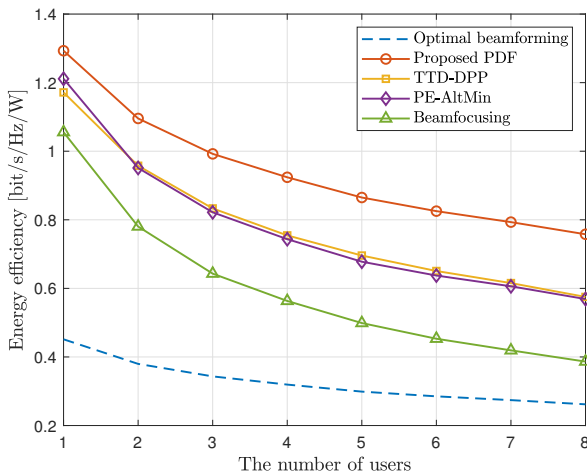


Fig. 12. Spectral efficiency w.r.t SNR.

Fig. 13. Energy efficiency w.r.t the number of users  $U$ .

are obtained through 10000 times Monte-Carlo simulations. With the increment of SNR, the spectral efficiency of our PDF method rises rapidly. When SNR = 10 dB, more than 3 bit/s/Hz improvement in spectral efficiency is achievable by the PDF method compared to the TTD-DPP method, which further strengthens the superiority of the PDF method.

### C. Energy Efficiency

Fig. 13 provides an energy efficiency comparison when  $U = N_{\text{RF}}$  varies from 1 to 8. The energy efficiency is defined as the ratio between the spectral efficiency and the total power consumed by the baseband digital processing and analog circuits. The compared benchmarks include the PE-AltMin [19] and narrowband beamfocusing [23] methods based on conventional hybrid beamforming (HB) architecture, the optimal beamforming based on the fully TTD (FTTD) arrays, and the TTD-DPP and PDF methods built on the DPP architecture. The power consumption of these three architectures, denoted by  $P_{\text{HB}}$ ,  $P_{\text{TTD}}$ , and  $P_{\text{DPP}}$  are given

by [21]

$$\begin{aligned} P_{\text{HB}} &= P_t + P_B + N_{\text{RF}}P_{\text{RF}} + N_{\text{RF}}NP_{\text{PS}}, \\ P_{\text{FTTD}} &= P_t + P_B + N_{\text{RF}}P_{\text{RF}} + N_{\text{RF}}NP_{\text{TTD}}, \\ P_{\text{DPP}} &= P_t + P_B + N_{\text{RF}}P_{\text{RF}} + N_{\text{RF}}NP_{\text{PS}} + N_{\text{RF}}KP_{\text{TTD}}, \end{aligned}$$

where  $P_t$  and  $P_B$  represent the transmission power and digital processing power, and  $P_{\text{RF}}$ ,  $P_{\text{PS}}$ , and  $P_{\text{TTD}}$  denote the power consumption of each RF chain, phase shifter, and TTD element. The following typical values are adopted:  $P_t = 30$  mW [21],  $P_B = 200$  mW [21],  $P_{\text{RF}} = 250$  mW [33],  $P_{\text{PS}} = 30$  mW [33], and  $P_{\text{TTD}} = 100$  mW [21]. The other settings are as follows: SNR = 5 dB;  $K = 8$ ;  $N = 256$ ;  $r_u \sim \mathcal{U}(1 \text{ m}, 30 \text{ m})$ ;  $\theta_u \sim \mathcal{U}(-\frac{\pi}{3}, \frac{\pi}{3})$ . It is clear from Fig. 13 that even though the optimal beamforming has the highest spectral efficiency, its energy efficiency is pretty low because of the large number of high-power TTDs used, i.e.,  $UN$ . In contrast, we can observe that the proposed PDF achieves much higher energy efficiency than all compared benchmarks. This observation is attributed to the fact that the PDF method can efficiently overcome the near-field beam-split effect with a quite small number of expensive TTDs, i.e.,  $UK \ll UN$ , which further demonstrates the efficacy of the proposed PDF method.

## VI. CONCLUSIONS

In this paper, we reveal an important challenge for future ELAA communications, i.e., the near-field beam split effect. To address this challenge, we first propose a piecewise-far-field model to approximate the near-field model with high accuracy. Applying this model, a PDF method is proposed to efficiently alleviate the near-field beam split effect through the joint manipulation of PSs and TDs. Moreover, we define a new metric called as “effective Rayleigh distance” by evaluating the beamforming gain, which is more accurate in quantifying the near-field range than the classical Rayleigh distance for practical communications. Finally, numerical results are provided to demonstrate the effectiveness of our work.

The discussion on the near-field beam split effect and our PDF method provide new vision to ELAA beamforming. Besides, our proposed effective Rayleigh distance offers a new way to evaluate the near-field range. For future works, people could investigate the near-field beam split effect in more general situations, such as multi-antenna users, uniform planar arrays, reconfigurable intelligent surfaces [34], and so forth. In addition, extending the effective Rayleigh distance to more applications deserves in-depth study as well.

## ACKNOWLEDGMENT

The authors sincerely thank Prof. Robert Schober and Prof. Lajos Hanzo for their valuable comments on this work.

## REFERENCES

- [1] R. W. Heath, N. González-Prelcic, S. Rangan, W. Roh, and A. M. Sayeed, “An overview of signal processing techniques for millimeter wave MIMO systems,” *IEEE J. Sel. Topics Signal Process.*, vol. 10, no. 3, pp. 436–453, Apr. 2016.

- [2] E. D. Carvalho, A. Ali, A. Amiri, M. Angjelichinoski, and R. W. Heath, "Non-stationarities in extra-large-scale massive MIMO," *IEEE Wireless Commun.*, vol. 27, no. 4, pp. 74–80, Aug. 2020.
- [3] "Radio stripes: re-thinking mobile networks," 2019. [Online]. Available: <https://www.ericsson.com/en/blog/2019/2/radio-stripes>.
- [4] W. Tang, M. Z. Chen, X. Chen, J. Y. Dai, Y. Han, M. Di Renzo, Y. Zeng, S. Jin, Q. Cheng, and T. J. Cui, "Wireless communications with reconfigurable intelligent surface: Path loss modeling and experimental measurement," *IEEE Trans. Wireless Commun.*, vol. 20, no. 1, pp. 421–439, Jan. 2021.
- [5] S. Nie, J. M. Jornet, and I. F. Akyildiz, "Intelligent environments based on ultra-massive MIMO platforms for wireless communication in millimeter wave and terahertz bands," in *Proc. IEEE ICASSP'19*, May 2019, pp. 7849–7853.
- [6] T. S. Rappaport, Y. Xing, O. Kanhere, S. Ju, A. Madanayake, S. Mandal, A. Alkhateeb, and G. C. Trichopoulos, "Wireless communications and applications above 100 GHz: Opportunities and challenges for 6G and beyond," *IEEE Access*, vol. 7, pp. 78 729–78 757, 2019.
- [7] H. Elayan, O. Amin, B. Shihada, R. M. Shubair, and M. Alouini, "Terahertz band: The last piece of RF spectrum puzzle for communication systems," *IEEE Open J. Commun. Soc.*, vol. 1, pp. 1–32, Jan. 2020.
- [8] M. Cui, Z. Wu, Y. Lu, X. Wei, and L. Dai, "Near-field MIMO communications for 6G: Fundamentals, challenges, potentials, and future directions," *IEEE Commun. Mag.*, vol. 61, no. 1, pp. 40–46, Jan. 2023.
- [9] Z. Zhou, X. Gao, J. Fang, and Z. Chen, "Spherical wave channel and analysis for large linear array in LoS conditions," in *Proc. IEEE Globecom Workshops 2015*, Dec. 2015, pp. 1–6.
- [10] B. Friedlander, "Localization of signals in the near-field of an antenna array," *IEEE Trans. Signal Process.*, vol. 67, no. 15, pp. 3885–3893, Aug. 2019.
- [11] D. Tse and P. Viswanath, *Fundamentals of Wireless Communication*. Cambridge, U.K.: Cambridge Univ. Press, 2005.
- [12] X. Li, Z. Dong, Y. Zeng, S. Jin, and R. Zhang, "Multi-user modular XL-MIMO communications: Near-field beam focusing pattern and user grouping," *arXiv preprint arXiv:2308.11289*, Aug. 2023.
- [13] K. T. Selvan and R. Janaswamy, "Fraunhofer and Fresnel distances: Unified derivation for aperture antennas," *IEEE Antennas Propag. Mag.*, vol. 59, no. 4, pp. 12–15, Aug. 2017.
- [14] H. Zhang, N. Shlezinger, F. Guidi, D. Dardari, and Y. C. Eldar, "6G wireless communications: From far-field beam steering to near-field beam focusing," *IEEE Commun. Mag.*, vol. 61, no. 4, pp. 72–77, Apr. 2023.
- [15] H. Sardeddeen, M.-S. Alouini, and T. Y. Al-Naffouri, "An overview of signal processing techniques for terahertz communications," *Proc. IEEE*, vol. 109, no. 10, pp. 1628–1665, Oct. 2021.
- [16] Y. Chen, Y. Xiong, D. Chen, T. Jiang, S. X. Ng, and L. Hanzo, "Hybrid precoding for wideband millimeter wave MIMO systems in the face of beam squint," *IEEE Trans. Wireless Commun.*, vol. 20, no. 3, pp. 1847–1860, Mar. 2021.
- [17] F. Sohrabi and W. Yu, "Hybrid analog and digital beamforming for mmWave OFDM large-scale antenna arrays," *IEEE J. Sel. Areas Commun.*, vol. 35, no. 7, pp. 1432–1443, Jul. 2017.
- [18] X. Liu and D. Qiao, "Space-time block coding-based beamforming for beam squint compensation," *IEEE Wireless Commun. Lett.*, vol. 8, no. 1, pp. 241–244, Feb. 2019.
- [19] X. Yu, J. Shen, J. Zhang, and K. B. Letaief, "Alternating minimization algorithms for hybrid precoding in millimeter wave MIMO systems," *IEEE J. Sel. Topics Signal Process.*, vol. 10, no. 3, pp. 485–500, Mar. 2016.
- [20] C. Lin, G. Y. Li, and L. Wang, "Subarray-based coordinated beamforming training for mmWave and sub-THz communications," *IEEE J. Sel. Areas Commun.*, vol. 35, no. 9, pp. 2115–2126, Sep. 2017.
- [21] L. Dai, J. Tan, Z. Chen, and H. V. Poor, "Delay-phase precoding for wideband thz massive MIMO," *IEEE Trans. Wireless Commun.*, vol. 21, no. 9, pp. 7271–7286, Sep. 2022.
- [22] A. Liao, Z. Gao, D. Wang, H. Wang, H. Yin, D. W. K. Ng, and M.-S. Alouini, "Terahertz ultra-massive MIMO-based aeronautical communications in space-air-ground integrated networks," *IEEE J. Sel. Areas Commun.*, vol. 39, no. 6, pp. 1741–1767, Jun. 2021.
- [23] D. Headland, Y. Monnai, D. Abbott, C. Fumeaux, and W. Withayachumnankul, "Tutorial: Terahertz beamforming, from concepts to realizations," *APL Photonics*, vol. 3, p. 051101, May 2018.
- [24] J. Sherman, "Properties of focused apertures in the Fresnel region," *IRE Trans. Antennas Propag.*, vol. 10, no. 4, pp. 399–408, Jul. 1962.
- [25] H. Zhang, N. Shlezinger, F. Guidi, D. Dardari, M. F. Imani, and Y. C. Eldar, "Beam focusing for near-field multiuser MIMO communications," *IEEE Trans. Wireless Commun.*, vol. 21, no. 9, pp. 7476–7490, Sep. 2022.
- [26] M. Cui, L. Dai, Z. Wang, S. Zhou, and N. Ge, "Near-field rainbow: Wideband beam training for XL-MIMO," *IEEE Trans. Wireless Commun.*, vol. 22, no. 6, pp. 3899–3912, Jun. 2023.
- [27] H. Hashemi, T. Chu, and J. Roderick, "Integrated true-time-delay-based ultra-wideband array processing," *IEEE Commun. Mag.*, vol. 46, no. 9, pp. 162–172, Sep. 2008.
- [28] B. Wang, F. Gao, S. Jin, H. Lin, G. Y. Li, S. Sun, and T. S. Rappaport, "Spatial-wideband effect in massive MIMO with application in mmwave systems," *IEEE Commun. Mag.*, vol. 56, no. 12, pp. 134–141, Dec. 2018.
- [29] R. J. Mailloux, *Phased Array Antenna Handbook*. Norwood, MA, USA: Artech House, 2005.
- [30] I. S. Gradshteyn and I. M. Ryzhik, *Table of Integrals, Series, and Products*. 8th ed. Boston, MA, USA: Academic, 2014.
- [31] M. Cui and L. Dai, "Channel estimation for extremely large-scale MIMO: Far-field or near-field?" *IEEE Trans. Commun.*, vol. 70, no. 4, pp. 2663–2677, Apr. 2022.
- [32] Z. Wu and L. Dai, "Multiple access for near-field communications: SDMA or LDMA?" *IEEE J. Sel. Areas Commun.*, vol. 41, no. 6, pp. 1918–1935, Jun. 2023.
- [33] R. Méndez-Rial, C. Rusu, N. González-Prelcic, A. Alkhateeb, and R. W. Heath, "Hybrid MIMO architectures for millimeter wave communications: Phase shifters or switches?" *IEEE Access*, vol. 4, pp. 247–267, 2016.
- [34] S. Yang, C. Xie, W. Lyu, B. Ning, Z. Zhang, and C. Yuen, "Near-field channel estimation for extremely large-scale reconfigurable intelligent surface (XL-RIS)-aided wideband mmwave systems," *arXiv preprint arXiv:2304.00440*, Apr. 2023.



**Mingyao Cui** received the B.E. and M.S. degrees in electronic engineering from Tsinghua University, Beijing, China, in 2020 and 2023, respectively. He is currently pursuing the Ph.D. degree in the University of HongKong. His research interests include massive MIMO, millimeter-wave communications, and near field communications. He received the IEEE ICC Outstanding Demo Award and the National Scholarship in 2022, and the HKPF Scholarship in 2023.



**Linglong Dai** (Fellow, IEEE) received the B.S. degree from Zhejiang University, Hangzhou, China, in 2003, the M.S. degree (with the highest honor) from the China Academy of Telecommunications Technology, Beijing, China, in 2006, and the Ph.D. degree (with the highest honor) from Tsinghua University, Beijing, China, in 2011. From 2011 to 2013, he was a Postdoctoral Research Fellow with the Department of Electronic Engineering, Tsinghua University, where he was an Assistant Professor from 2013 to 2016, an Associate Professor from

2016 to 2022, and has been a Professor since 2022. His current research interests include massive MIMO, reconfigurable intelligent surface (RIS), millimeter-wave and Terahertz communications, near-field communications, machine learning for wireless communications, and electromagnetic information theory.

He has coauthored the book *MmWave Massive MIMO: A Paradigm for 5G* (Academic Press, 2016). He has authored or coauthored over 100 IEEE journal papers and over 60 IEEE conference papers. He also holds over 20 granted patents. He has received five IEEE Best Paper Awards at the IEEE ICC 2013, the IEEE ICC 2014, the IEEE ICC 2017, the IEEE VTC 2017-Fall, the IEEE ICC 2018, and the IEEE GLOBECOM 2023. He has also received the Tsinghua University Outstanding Ph.D. Graduate Award in 2011, the Beijing Excellent Doctoral Dissertation Award in 2012, the China National Excellent Doctoral Dissertation Nomination Award in 2013, the URSI Young Scientist Award in 2014, the IEEE Transactions on Broadcasting Best Paper Award in 2015, the Electronics Letters Best Paper Award in 2016, the National Natural Science Foundation of China for Outstanding Young Scholars in 2017, the IEEE ComSoc Asia-Pacific Outstanding Young Researcher Award in 2017, the IEEE ComSoc Asia-Pacific Outstanding Paper Award in 2018, the China Communications Best Paper Award in 2019, the IEEE Access Best Multimedia Award in 2020, the IEEE Communications Society Leonard G. Abraham Prize in 2020, the IEEE ComSoc Stephen O. Rice Prize in 2022, the IEEE ICC Outstanding Demo Award in 2022, and the National Science Foundation for Distinguished Young Scholars in 2023. He was listed as a Highly Cited Researcher by Clarivate Analytics from 2020 to 2023. He was elevated as an IEEE Fellow in 2022.